Bio-Inspired Artificial Vision and Neuromorphic Image Processing Devices

Min Sung Kim, Min Seok Kim, Gil Ju Lee, Sung-Hyuk Sunwoo, Sehui Chang, Young Min Song,* and Dae-Hyeong Kim*

Remarkable technological developments for efficient image recognition (i.e., image acquisition and image data processing) have been reported in the past decade. Such advances in imaging and image processing technologies have driven significant progress in mobile electronics and machine vision applications. In particular, for image acquisition devices, two types of natural eyes (i.e., chambered and compound eyes) have inspired the development of novel multifunctional imaging devices with unique optical geometries. For image data processing devices, novel computing devices based on memristor crossbar arrays, such as electronic synapses, have been developed. More recently, the integration of imaging and image processing devices in a single unit further enhances the system-level efficiency. Herein, such recent advances in the bio-inspired artificial vision and neuromorphic image processing devices, aimed at providing efficient image recognition, are reviewed. First, various imaging devices inspired by the structural and functional features of natural eyes are introduced. Second, artificial synapses and their operation principles are thoroughly discussed. Third, the neuromorphic vision sensor that integrates the imaging and image processing devices is reviewed. Finally, a brief summary and future outlook are presented.

1. Introduction

Recent progress in mobile electronics and machine vision has increased the demand for advanced image acquisition and

M. Su. Kim, S.-H. Sunwoo, Prof. D.-H. Kim
Center for Nanoparticle Research
Institute for Basic Science (IBS)
Seoul 08826, Republic of Korea
E-mail: dkim98@snu.ac.kr
M. Su. Kim, S.-H. Sunwoo, Prof. D.-H. Kim
School of Chemical and Biological Engineering
Institute of Chemical Processes
Seoul National University
Seoul 08826, Republic of Korea
M. Se. Kim, Dr. G. J. Lee, S. Chang, Prof. Y. M. Song
School of Electrical Engineering and Computer Science
Gwangju Institute of Science and Technology
Gwangju 61005, Republic of Korea
E-mail: ymsong@gist.ac.kr
Prof. D.-H. Kim
Department of Materials Science and Engineering
Seoul National University
Seoul 08826, Republic of Korea

The ORCID identification number(s) for the author(s) of this article can be found under https://doi.org/10.1002/admt.202100144.

processing devices.[1–6] However, conventional image recognition systems using a flat image sensor array with a multilens optical system and the von-Neumann computing architecture for processing the acquired image data have several limitations such as high system-level complexity, bulky module size, large computing load, and low energy efficiency.[7] Therefore, advanced devices in both image acquisition and image data processing are required. As a result, bio-inspired imaging devices[8–10] (i.e., artificial vision) and neuromorphic image processing devices[11–13] (i.e., artificial synapse) have received considerable attention (**Figure 1**).

Bio-inspired imaging devices (e.g., bio-inspired camera) have been developed for image acquisition.[14] Conventional imaging devices require bulky and heavy optical systems to obtain high-quality visual information.[15] In contrast, natural eyes have a simple and small optical geometry and high-quality image acquisition capability.[16,17] Therefore, bio-inspired artificial vision has been developed by mimicking the unique structural and functional advantage of natural eyes[2,6] (Figure 1a). For example, the chambered eye, typically found in humans and aquatic animals, exhibits a wide field of view, low optical aberration, and facile accommodation with a simple optical system.[16,17] The compound eye has distinctive optical geometries, and such structures offer various useful visual features.[18,19]

Neuromorphic computing devices that can efficiently process massive image data acquired from the imaging device have been developed for image data processing.[20–22] The conventional von-Neumann architecture, in which the central processing unit and memory unit are separated, is not suitable to efficiently process the massive unstructured image data.[23,24] Therefore, a novel computing device inspired by the human brain (i.e., electronic synapse) has been developed[25,26] (Figure 1b). For example, the memristor crossbar array can efficiently perform vector multiplications.[27] Such a neuromorphic device implements artificial neural networks (ANN) in the hardware and enables efficient parallel processing of image data with low energy consumption.[25] In a previous study, a device that integrates the synaptic device and photodetector in one unit has been reported.[26]

Despite recent progress in the hardware of the neuromorphic image data processing devices, such devices still require
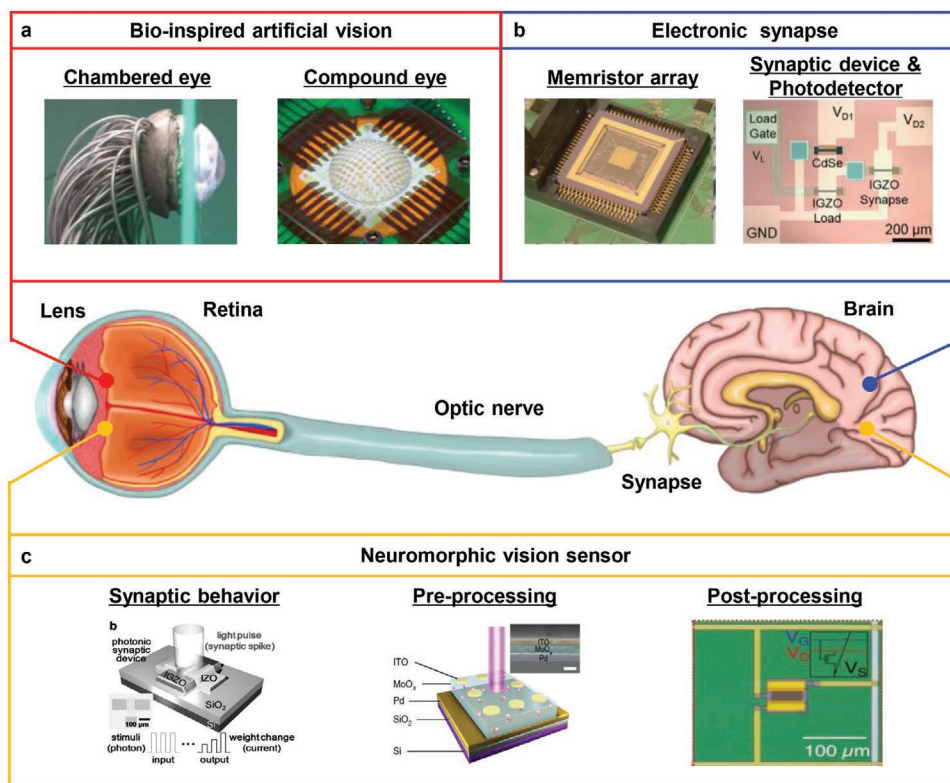
Figure 1. a) Various imaging and image processing devices inspired by the human visual system, such as bio-inspired artificial vision, b) electronic synapse, and c) neuromorphic vision sensor. With the pre-processing device, an image with a higher contrast and a lesser noise can be produced. The post-processing device extracts features from the pre-processed image data for additional data processing and recognition of the image. a) Reproduced with permission.[80] Copyright 2020, Springer Nature (left). Reproduced with permission.[41] Copyright 2013, Springer Nature (right). b) Reproduced with permission.[25] Copyright 2017, Springer Nature (left). Reproduced with permission.[26] Copyright 2019, Wiley-VCH Verlag GmbH & Co. KGaA. c) Reproduced with permission.[29] Copyright 2018, Wiley-VCH Verlag GmbH & Co. KGaA. Reproduced with permission.[30] Copyright 2019, Springer Nature (center). Reproduced with permission.[31] Copyright 2020, Wiley-VCH Verlag GmbH & Co. KGaA (right).

additional image sensors to acquire image information.[5] This inevitably introduces high system-level complexity and requires data communication.[28] Therefore, integrating an image sensing device with a neuromorphic image processing device (i.e., neuromorphic vision sensor) has been proposed[29–31] (Figure 1c). The neuromorphic vision sensor exhibits light-responsive synaptic behavior, such as short-term plasticity (STP), long-term plasticity (LTP), and spike-timing-dependent plasticity (STDP).[29] In addition, by emulating the human visual system, a neuromorphic vision sensor that can perform both pre-processing[30] and post-processing[31] of the image data has been developed.

Herein, we review recent advances in the bio-inspired artificial vision and neuromorphic image processing devices, which aim for efficient image recognition. First, we introduce the bio-inspired imaging devices that mimic structural and functional advantages of natural eyes (i.e., chambered eyes and compound eyes). Second, we discuss the artificial synapses (i.e., electronic synapses), which are inspired by the image data processing of the human brain. Third, we review the neuromorphic vision sensor, which integrates the image sensing and neuromorphic image data processing devices in a single unit. Finally, we briefly summarize the current state of the bio-inspired artificial vision and neuromorphic image processing device and present their future outlook.

2. Bio-Inspired Artificial Vision System

Modern imaging systems play a vital role in various fields such as unmanned drones, autonomous driving, augmented reality, and virtual reality.[1,32] There is a need to incorporate additional features to these imaging systems, such as a wide FoV, 3D real-time depth sensing capability, and hyperspectral imaging function[33,34] (i.e., infrared (IR), visible (vis), and ultraviolet (UV)). However, to obtain such features, the conventional imaging systems require bulky optics and/or additional complex components such as multilens optics, multiple cameras, and color filter arrays.[35,36] To address these issues, many systems with novel structures that are inspired by intriguing eye structures in nature have been reported.[16,17,32,37]

In particular, the curved image sensor array is a remarkable outcome of mimicking the natural eye.[38] For example, the imaging systems inspired by the chambered eyes enabled low aberration and high resolution[39,40] (**Figure 2**; i,ii), and those inspired by the compound eyes achieved infinite depth of field (DoF) and wide FoV[41–43] (Figure 2; iii,iv). Recently, the bio-inspired imaging systems that imitate special features and functions of natural eyes, such as optical, photonic, and mechanical structures, have been reported.[34,44] For example, in the case of chambered eyes, the ball lenses and typical
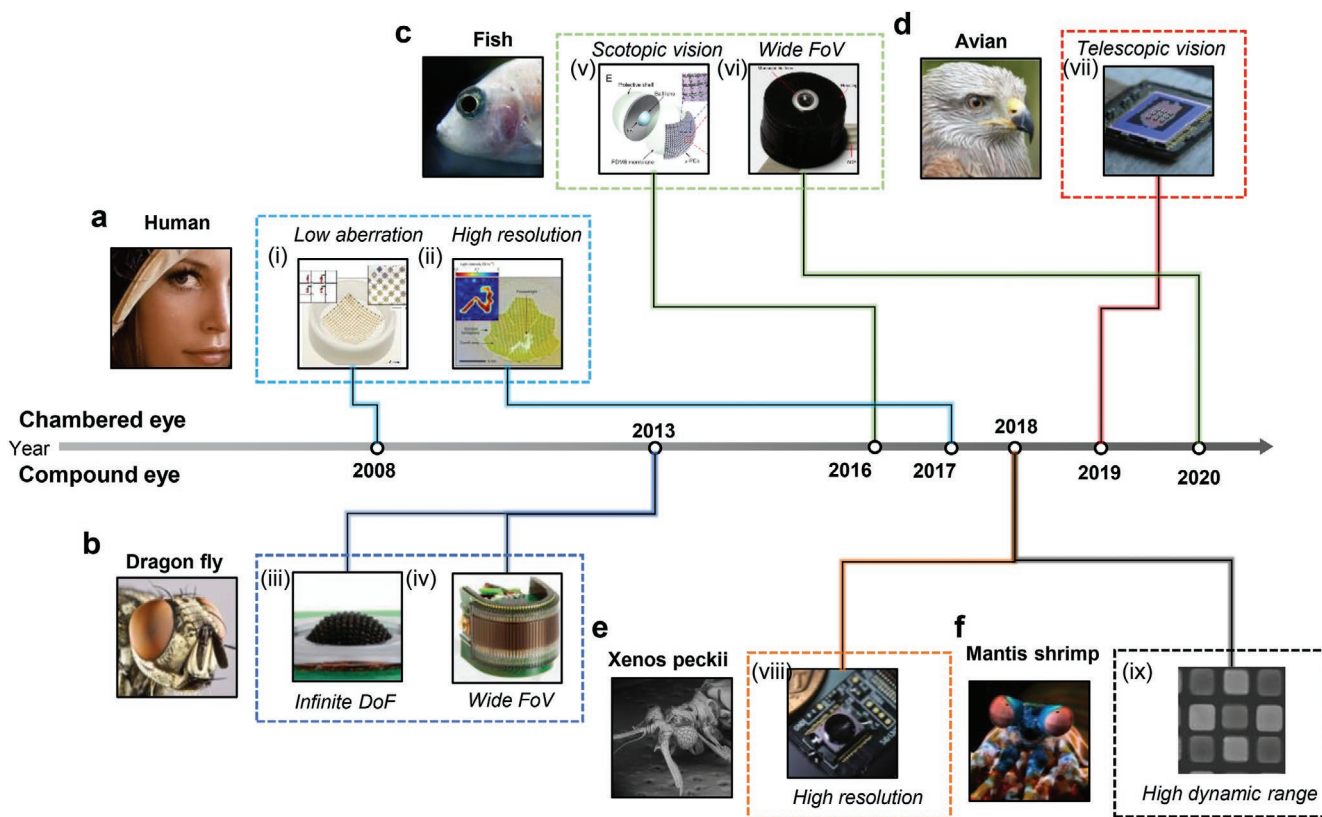
**ADVANCED
SCIENCE NEWS**
www.advancedsciencenews.com

**ADVANCED
MATERIALS
TECHNOLOGIES**
www.advmattechnol.de

Figure 2. Various natural and artificial vision systems. a) Picture of human eye. i) Curved image sensor using compressible metal interconnection, ii) curved image sensor using soft 2D materials. b) Dragon-fly-eye-inspired vision system. iii) Arthropod-eye-inspired system based on stretchable metal connections and elastomeric micro-lenses. iv) One directional wide field of view imaging system using a flexible printed circuit board. c) Vision system inspired by aquatic creature eye. v) Elephantnose-fish-inspired vision system for imaging under dim environment. vi) Artificial vision system with a monocentric lens inspired by the fisheye. d) Avian vision system. vii) Artificial vision system with 3D-printed micro relay lenses for telescopic imaging. e) Superposition type compound eye vision for information sharing. viii) Small-form factor vision system inspired by Xenos peckii. f) Picture of mantis shrimp. ix) The scanning electron microscopy image shows the pixelated polarization filter for the mantis-shrimp-eye-inspired vision system. b) Reproduced with permission.[43] Copyright 2013, Springer Nature. c) Reproduced with permission.[45] Copyright 2020, Springer Nature. d) Reproduced with permission.[47] Copyright 2020, Springer Nature. e) Reproduced with permission.[48] Copyright 2018, Springer Nature. f) Reproduced with permission.[114] Copyright 2016, Springer Nature. i) Reproduced with permission.[39] Copyright 2008, Springer Nature. ii) Reproduced with permission.[40] Copyright 2017, Springer Nature. iii) Reproduced with permission.[41] Copyright 2013, Springer Nature. iv) Reproduced with permission.[42] Copyright 2015, National Academy of Sciences. v) Reproduced with permission.[44] Copyright 2015, National Academy of Sciences. vi) Reproduced with permission.[45] Copyright 2020, Springer Nature. vii) Reproduced with permission.[46] Copyright 2017, American Association for the Advancement of Science. viii) Reproduced with permission.[48] Copyright 2018, Springer Nature. ix) Reproduced with permission.[49] Copyright 2017, The Optical Society.

mechanical functions of aquatic organisms[44,45] (Figure 2; v,vi) and the telescopic vision of birds[46,47] (Figure 2; vii) have been mimicked. In the case of compound eyes, the visual system of Xenos peckii for recognizing image depth and enhancing sensitivity[48] (Figure 2; viii) and various optical filters of mantis shrimp for distinguishing two similar colors[49] (Figure 2; ix) have been mimicked. Therefore, mimicking unique features of natural eyes can be a potential solution to overcome the limitations of the conventional imaging systems. This section reviews the unique imaging systems that are inspired by various natural eyes.

2.1. Chambered-Eye-Inspired Artificial Vision

The chambered eye, typically found in humans and aquatic animals, consists of a curved retina, a gradient-index crystalline lens, and a tunable iris.[50–52] Despite its remarkably simple configuration, it exhibits high-performance imaging capabilities[14] (e.g., wide FoV, low aberration, and facile accommodation). Each optical component of the chambered eye has evolved to favor the survival of an organism in its own habitat environment.[53] For instance, the human eye possesses an aspherical crystalline lens with a graded refractive index (GRIN) to compensate for the optical aberrations.[54] In contrast, a spherical GRIN lens, which can be found in many aqueous animals, enables high-quality underwater vision that collects a panoramic scene with minimum aberrations owing to its spherical shape.[55]

One of the main features of the chambered eye is the curved retina that facilitates high-resolution imaging with a wide FoV and low optical aberrations, while allowing simple configuration of the optical system[53] (**Figure 3**a). In the past few decades, various approaches for obtaining artificial curved retina,
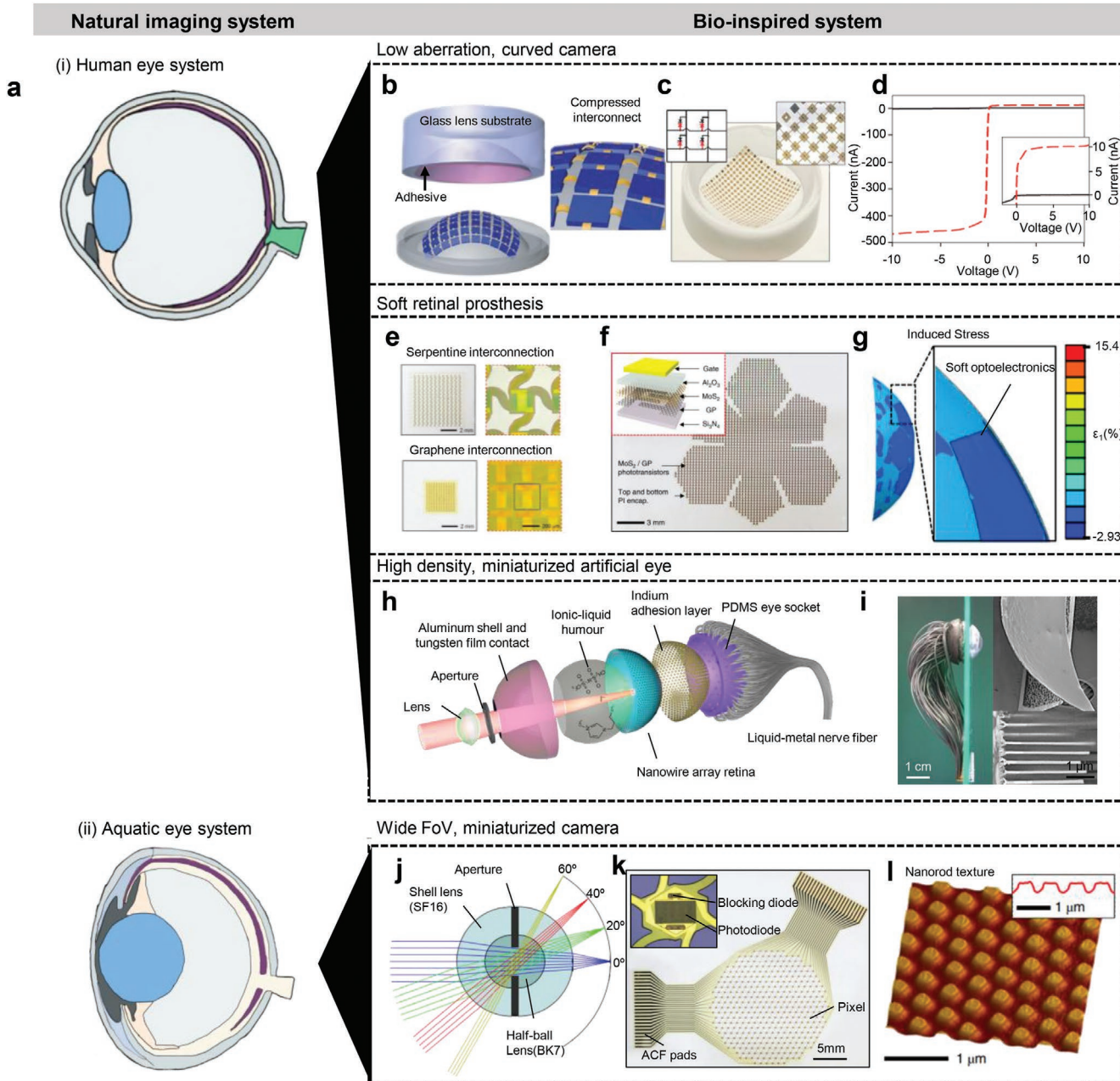
Figure 3. a) Various chambered-eye-type vision systems such as i) human-eye-type and ii) aquatic-eye-type system. b) Illustration of the fabrication method for the curved image sensor with compressible metal interconnections. c) Picture of the fabricated curved imaging system. Each pixel consists of a blocking diode and a photodiode (inset). d) Current and voltage curve. e) Metal interconnection for curved image sensor. Serpentine-shape metal interconnection (top) shows low density and graphene interconnection improves pixel density (bottom). f) Photograph of the fabricated curved image sensor with soft 2D materials such as MoS_2 and graphene. g) Induced strain on the curved soft optoelectronics. h) Artificial hemispherical vision system with high density photosensitive perovskite nanowires. i) The fabricated artificial eye (left) and the scanning electron microscopy image of perovskite nanowires (right). j) Cross-sectional illustration of fisheye-inspired artificial vision system. k) Array of hexagonal pixels that consist of a photodetector and a blocking diode (inset) with serpentine metal connections. l) Atomic Force Microscopy image of the texture on the photodetector surface. b–d) Reproduced with permission.[39] Copyright 2008, Springer Nature. e–g) Reproduced with permission.[40] Copyright 2017, Springer Nature. h,i) Reproduced with permission.[80] Copyright 2020, Springer Nature. j–l) Reproduced with permission.[45] Copyright 2020, Springer Nature. a; i) Reproduced with permission.[40] Copyright 2017, Springer Nature. a; ii) Reproduced with permission.[45] Copyright 2020, Springer Nature.

such as mesh-based pixel array design,[56–58] thin complementary metal-oxide-semiconductor (CMOS) image sensor array,[59,60] and image sensor array fabricated by origami and/or kirigami methods[61–64] have been proposed.

For example, Ko et al. reported an electronic eye that was based on a curved silicon image sensor array with an isolated pixel design[39] (Figure 3b). Conventional microfabrication processes are used to fabricate a passive matrix image sensor array

that consists of silicon photodiodes, current-blocking diodes, and electrodes with polyimide encapsulation. Further, the isolated pixels are connected by a compressible metal interconnection that can endure a compressive strain of >50%[39] (Figure 3b, inset). The compressible metal interconnection facilitates transferring of the planar device to a substrate with a nearly hemispherical shape (Figure 3c, inset, right). Each pixel in the 16×16 image sensor array is composed of two devices: photodetecting and blocking diodes (Figure 3c; inset, left). The former detects light, and the latter minimizes crosstalk in the passive matrix. Hence, under reverse bias, the current–voltage curve of photodiode and blocking diode shows a truncated shape (the feature of bipolar junction transistor) with a high on/off ratio and low leakage currents (Figure 3d). Although the compressive metal interconnection allows the fabrication of a curved image sensor array, such a mesh design has limitations in achieving the high pixel density and high array deformability.[65]

Another strategy to fabricate the curved image sensor is to introduce the serpentine-shaped metal interconnection to enhance degree of freedom for geometrical structure.[66–72] The serpentine-shaped interconnection allows the array to be stretchable,[73–79] and thus makes a conformal contact on the curved surface (Figure 3e, top). However, this serpentine-shaped design still has a low pixel density of the array. Several researches have been conducted to overcome this issue of low pixel density.[59,80] For example, Choi et al. developed a curved image sensor array based on a heterostructure of MoS_2 and graphene and used the kirigami method for designing the array[40] (Figure 3e, bottom; Figure 3f). The kirigami-based array design allows transferring the high-density image sensor array from a planar surface to a curvilinear surface while minimizing the mechanical stress.[61–64,81–85] Furthermore, the ultrathin and soft 2D materials (i.e., MoS_2 and graphene) help in preventing mechanical fractures of the array on a hemispherical surface. The photodetector exhibited high photoabsorption efficiency[40] ($>5 \times 10^7$ m^{-1}), photoresponsibility[40] ($\approx$2200 A W^{-1}), and fracture strain[40] ($\approx$23%), and the curved image sensor array could be conformally integrated on a hemispherical surface with small induced strains (Figure 3g).

The 2D fabrication process imposes limitations in terms of pixel density when implementing a curved image sensor. Therefore, 3D fabrication method is one of the strategies to achieve high pixel density on curved surfaces. Several 3D fabrication methods have been proposed to directly fabricate pixel arrays on a curved platform.[86,87] For example, 3D printing with a semiconducting polymer ink was used to fabricate organic photodetectors with a 3D geometry.[88] More recently, Gu et al. fabricated a dense array of perovskite nanowires on a hemispherical substrate, known as electrochemical eye (EC-EYE), using a direct vapor-phase nanowire growth method on a 3D platform.[80] The EC-EYE consists of a single lens, an aperture, an artificial retina, and liquid metal wirings (Figure 3h). The key feature of the EC-EYE is the artificial retina that is composed of a dense array of light-sensitive nanowires[80] (pitch of 500 nm, density of 4.6×10^8 cm^{-2}) in the pores of an aluminum oxide membrane (Figure 3i). Each nanowire mimics a photoreceptor cell in the human retina. The gallium-indium liquid metal wires in flexible polymer tubes, which mimic the human nerve fibers, are used for the photocurrent transmission

between the nanowires and an external current meter. A polydimethylsiloxane (PDMS) membrane holds the artificial retina by supporting the firm electrical contacts between the nanowires and the liquid metal wires. The indium layer between the liquid metal and the nanowires enhances the quality of the electrical contacts. The EC-EYE has the diagonal FoV of $\approx$100.1°, which can be improved up to $\approx$130° by optimizing the pixel distribution on the hemispherical retina.[80]

Meanwhile, an artificial vision inspired by an aquatic animal was reported by Kim et al.[45] The unique optical structure of the aquatic eye, such as a monocentric lens brings exceptional optical characteristics—deep DoF and panorama FoV. Furthermore, the retractor/protractor muscle of the eye of an aquatic animal is also a unique component, which is distinct from that of a land creature. The spherical monocentric GRIN lens has a short focal length and deep DoF. Different from the human eye that relaxes and contracts the ciliary muscle to focus on the target object, an aqueous organism uses the retractor/protractor muscle to move the lens backward and forward to adjust the focus. To mimic the monocentric GRIN lens of the aqueous vision, a spherical monocentric ball lens is fabricated by integrating an SF16 shell lens and a BK7 hemispherical lens (Figure 3j). As a curved artificial retina, silicon-based photodiodes and blocking diodes are arranged in a hexagonal mesh that is interconnected by the serpentine-shaped metal lines (Figure 3k). The mesh array design with the serpentine interconnections helps in reducing the induced strain in the array that is mounted on a hemispherical substrate.[89–102] As aquatic creatures have elongated rod cells for high light sensitivity under the sea, the silicon photodiodes have nanotextures that can increase the light absorption efficiency of each photodiode by reducing the reflection and increasing the absorption (Figure 3l).

2.2. Compound-Eye-Inspired Artificial Vision

The compound eyes, which can be categorized into apposition and superposition types, consist of an array of hundreds of thousands of ommatidia. Each ommatidium—a minimal optical sensing unit—comprises a facet lens, crystalline cone, light-guiding rhabdom, and photoreceptor cells.[103,104] Unlike the chambered eye, where the photoreceptor is settled on a concave geometry, the compound eye has a photoreceptor array on a convex geometry.[16,17] Owing to such an array configuration of multiple optical units (i.e., ommatidia), the compound eye exhibits the infinite DoF, wide FoV, fast object detection capability, and full-color 3D sensing capability.[16,17] With the advances in novel nanofabrication methods, the fabrication of the advanced imaging systems that mimic exceptional optical features of the compound eye has been achieved.

Figure 4a shows five types of compound eye in nature: i) apposition, ii) neural superposition, iii) refracting superposition, iv) reflecting superposition, and v) parabolic superposition. Each type of compound eye is found in various species of insects based on their natural habits[103,104] (i.e., diurnal and nocturnal habits). The apposition-type compound eyes are commonly found in diurnal insects, which act effectively under abundant light conditions. In contrast, nocturnal insects, which
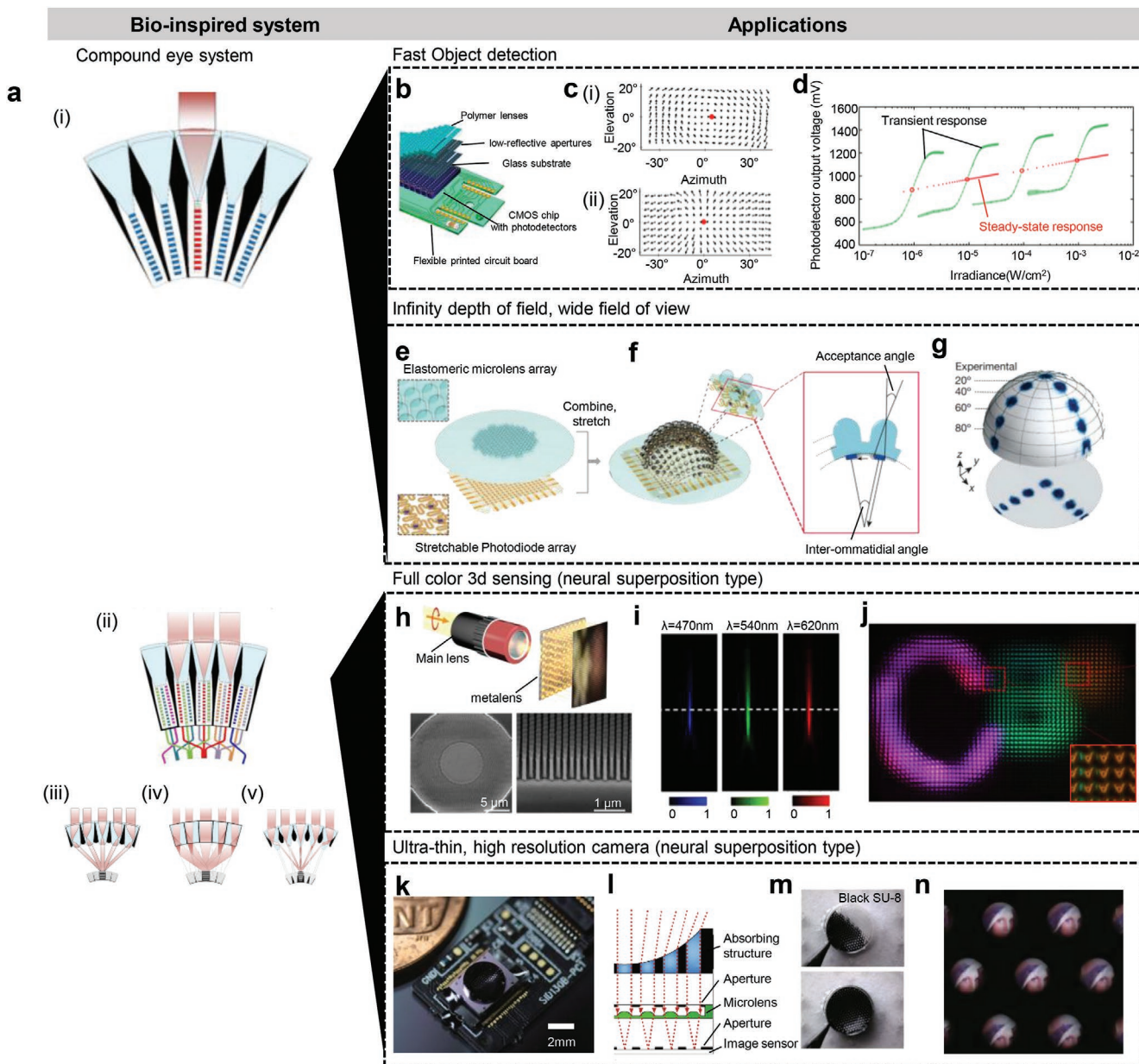
**ADVANCED
SCIENCE NEWS**

www.advancedsciencenews.com

**ADVANCED
MATERIALS
TECHNOLOGIES**

www.advmattechnol.de

Figure 4. a) Various compound-eye-type vision systems. i) Apposition type, ii) Neural superposition type, iii) Refracting type, iv) Reflecting type, and v) Parabolic type. b) Illustration of wide field-of-view compound eye system using a flexible printed circuit board. c) The result of the optical flow method for the roll motion and linear translation. d) Transient response and steady-state response with the auto-adaptation function. e) Illustration of the elastomeric microlens array and stretchable electronics for the compound-eye-type artificial vision. f) Illustration of the curved apposition-type artificial vision. Each microlens limits the acceptance angle. g) Experimental result of the wide field-of-view imaging. h) Light field camera system with the metalens array for light information sharing (top) and scanning electron microscopy images of the metalens (bottom). i) Achromatic characteristics of the fabricated metalens array. j) Captured image with the light field camera system. k) Ultra-thin compound eye camera. l) Illustration of the microprism system for wide field-of-view. m) Black SU-8 aperture for removal of the optical crosstalk. n) Obtained image with the ultrathin compound eye camera. b–d) Reproduced with permission.[42] Copyright 2013, National Academy of Sciences. e–g) Reproduced with permission.[41] Copyright 2013, Springer Nature. h–j) Reproduced with permission.[112] Copyright 2019, Springer Nature. k–n) Reproduced with permission.[48] Copyright 2018, Springer Nature. i–v) Reproduced with permission.[104] Copyright 2016, Springer Nature.

inhabit under dim light conditions, generally have superposition-type compound eyes. Since each adjacent ommatidium in the superposition-type compound eye shares the same light information, the light sensitivity in this case can be improved.

Several compound-eye-type artificial visions have been developed to exploit the advantages of the compound eye such as

minimal optical aberration, extremely wide FoV, infinite DoF, and compact configuration. Novel microfabrication techniques allow the implementation of microlens array (MLA) and black pigments on the conventional image sensor to fabricate the artificial ommatidium.[103] However, the planar configuration of the conventional image sensor array restricts the implementation

**ADVANCED
SCIENCE NEWS**

www.advancedsciencenews.com

**ADVANCED
MATERIALS
TECHNOLOGIES**

www.advmattechnol.de

of the full panoramic FoV of the compound eye.[18,19,105–107] In this aspect, one of the major challenges in fabricating the compound-eye-type imaging devices is to achieve a high curvature in various imaging elements (i.e., photodiodes array, phototransistors array, and MLA fabricated on a highly curved 3D substrate).

One strategy to realize a curved photodetector array is to use a flexible printed circuit board (FPCB). The photodiodes on the FPCB allow various shape deformations and resultant variations in the FoV.[108] Moreover, the CMOS image sensors can be sliced and integrated on the FPCB to fabricate the curved artificial compound eye[42] (CurvACE). Such a CurvACE can achieve a wide 1D FoV (Figure 4b). The main goal of the CurvACE is to achieve the fast object detection and the extraction of motion information with the optical flow method (Figure 4c; i,ii). In addition, the auto-adaptation function can be used to keep the photodetectors responsive toward relative brightness changes even under intense ambient lighting conditions (Figure 4d). The prototype of the CurvACE[42] consists of 630 photodiodes with a vertical FoV of 60°.

To overcome the limited FoV, the serpentine-shaped stretchable metal interconnection was utilized to fabricate an artificial hemispherical compound eye with a fully hemispherical FoV[41] (Figure 4e). A passive matrix silicon image sensor array, which consists of photodiodes and blocking diodes, was interconnected by the serpentine metal electrodes. The optical subsystem is composed of a PDMS MLA and a light-screening layer. Although the FoV of an individual pixel is limited by the acceptance angle, the hemispherical configuration of the pixels, including the microlenses, can offer a wide FoV (Figure 4f). For the artificial compound eye, the experimental results prove the imaging capability with a wide hemispherical FoV[41] (=160°) (Figure 4g). This apposition-type compound eye also features individualized imaging, low optical aberrations, and almost infinite DoF.

Meanwhile, the superposition-type compound eyes also have attractive optical characteristics such as high light sensitivity, depth sensing capability, and high dynamic range.[16,104] The refracting, reflecting, and parabolic superposition type can collect light using the adjacent optical units, which enhances the light sensitivity even under a dim environment. For example, Huang et al. reported micro-square tubes with reflecting sidewalls inspired by the reflecting superposition-type compound eye found in decapods such as shrimps, lobsters, and crayfish.[109] Furthermore, the ommatidia of the superposition-type compound eye share the object information such as position, color, and intensity, which enables the recognition of the depth information. The shared FoV of multiple ommatidia is similar to the principle of a light field camera[110] (Figure 4h, top). However, images from a single microlens in the superposition-type compound eye inherently undergo achromatic and spherical aberrations. Therefore, Lin et al. replaced the conventional microlens with a metalens that can capture a broadband achromatic image with no spherical aberration[111] (Figure 4h, bottom; Figure 4i). Among the dielectric materials used in the metalens, GaN has advantages such as lower manufacturing cost and higher efficiency than silicon and titanium oxide. A single achromatic metalens consists of more than 9000 GaN nanoantennas, and it is fabricated using electron beam lithography,

several transfer processes, and etching processes. An imaging system with field-sharing characteristics, which is the main feature of the superposition-type compound eye, exhibits low chromatic aberration and no spherical aberration (Figure 4j).

To mimic the neural superposition-type compound eye, an MLA was integrated with a wafer-level camera without a main optical system. The MLA allows achieving an acceptable sensitivity and integrating the aperture-stacked structures with minimal optical crosstalk.[8] For example, Kim et al. reported a Xenos peckii-eye-inspired ultrathin digital camera[48] (Figure 4k). The ultrathin digital camera is equipped with a microprism array that refracts light from wide viewing angles to achieve a wide FoV, a light-blocking structure and aperture that minimize optical crosstalk between the adjacent channels, and an MLA that focuses light on the CMOS image sensor (Figure 4l). The main element of the ultrathin digital camera is the concave microprism array. Owing to the microprism array, the ultrathin digital camera features a FoV of 68° with a device thickness of 1.4 mm. A light-screening structure is fabricated by a capillary filling method using black epoxy (e.g., SU-8) (Figure 4m). For high-resolution imaging, the images that were originally captured from the microprism arrays were reconstructed using a super-resolution method (Figure 4n).

2.3. Artificial Vision Inspired by the Photonic Structures of Natural Eyes

Diverse structures of natural eyes have inspired novel devices for the artificial vision with unique features such as low optical aberration, excellent focusing capability, wide FoV, deep DoF, and small module sizes.[112] Recently, thorough analyses on the extraordinary photonic structures of natural eyes, such as the orthogonal microvilli of mantis shrimp, layered retina of jumping spider, crystalline microcups with reflecting photonic crystal sidewalls of elephant nose fish, and tapetum lucidum of ommatidia of morpho butterfly, have encouraged further researches on bio-inspired artificial vision[34,37,113,114] (**Figure 5**a; i–iv).

Mantis shrimp has one of the most complex and distinct optical systems among the variety of natural eyes. It can detect 16 multispectral wavelengths, two circular polarized lights, and four linear polarized lights[49,115] (Figure 5b). The individual photoreceptors of the mantis shrimp have a logarithmic photoresponse;[115] hence, each photoreceptor can distinguish light intensity levels even under strong ambient light conditions. Garcia et al. demonstrated a mantis shrimp-inspired CMOS image sensor array with pixelated polarization filters. In this CMOS image sensor array, 2×2 pixelated polarization filters with an offset of 45° are repeated across the pixel array for the detection of the polarized light (Figure 5c). An individual pixel has a polarization filter which is composed of aluminum nanowires with a duty cycle of 50% in dimensions of 250 nm × 75 nm. For imaging with a high dynamic range, the photodiode is designed to operate in a forward bias mode, unlike conventional photodetectors that operate in a reverse bias mode. The customized pixel follows a logarithmic photoresponse like the photoreceptors in the mantis shrimp eye (Figure 5d). Therefore, the mantis shrimp-inspired image sensor array can provide the
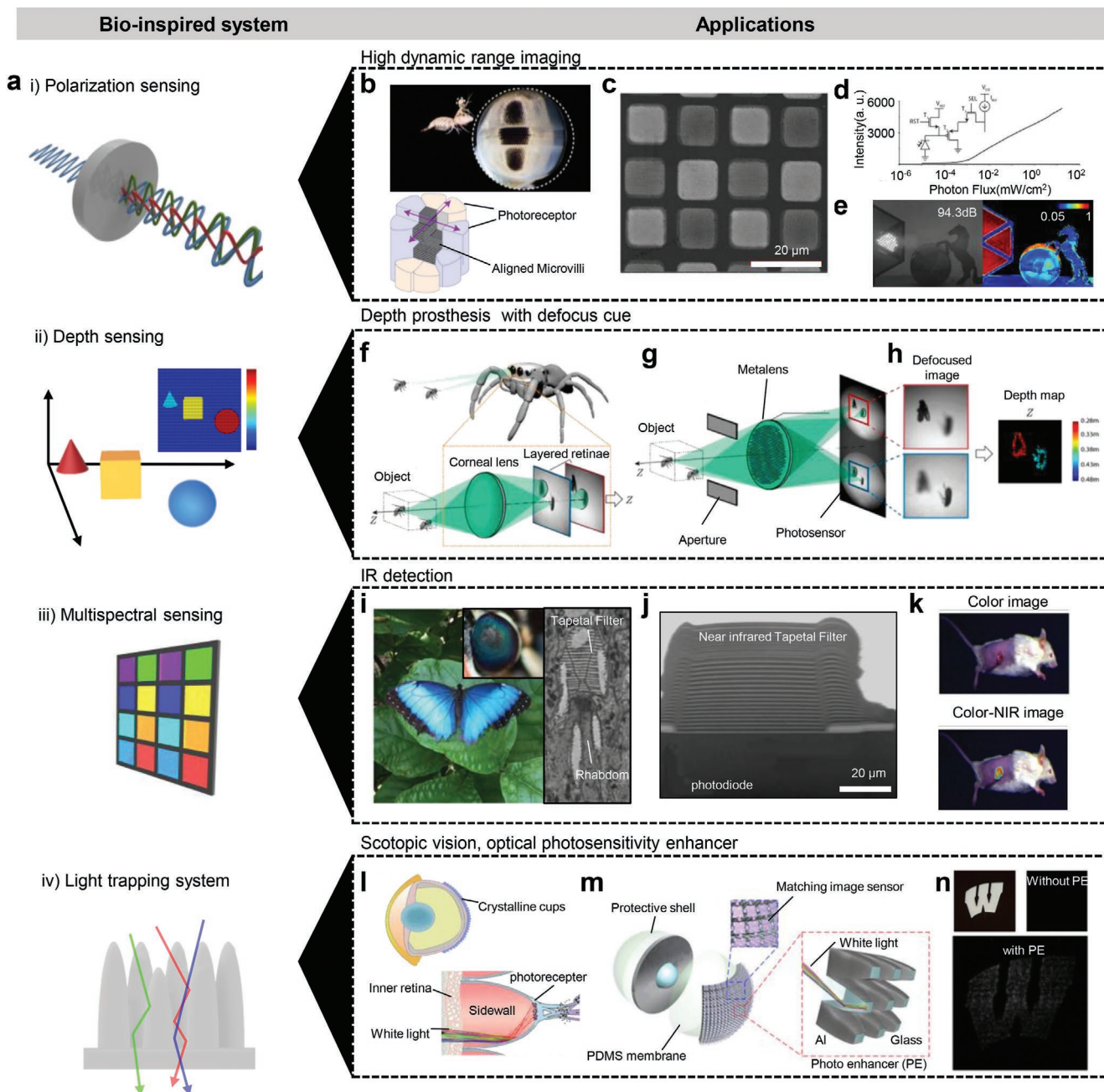
**ADVANCED
SCIENCE NEWS**

www.advancedsciencenews.com

**ADVANCED
MATERIALS
TECHNOLOGIES**

www.advmattechnol.de

Figure 5. a) Diverse optical and photonics structure for multifunctional imaging in the nature eye: i) polarization sensing, ii) depth sensing, iii) multi-spectral imaging, and iv) light enhancing system. b) Polarization filter (bottom) in the mantis shrimp ommatidia. c) Scanning electron microscopy image of the fabricated polarization filter. d) Graph of digitized intensity and photon flux. e) The image obtained by the device shows the high dynamic range and polarization sensitive characteristics. f) Illustration of the depth perception mechanism of jumping spider. The layered retina captures two images which have different focal length. g) Concept of a proposed method for the alternative depth sensing inspired by jumping spider. h) Two defocused images, which can generate a depth map. i) Optical filter (right) for wavelength selection in Morpho butterfly (left). j) Fabricated multilayered film for the Infrared filter on the CMOS image sensor. k) Captured image without the optical filter (top) and with a bio-inspired filter (bottom). l) Illustrations that describe features of the elephantnose fish retina, which has a micro mirror cup for imaging under dim environment. m) Proposed artificial micro cup for light guiding and trapping. n) Original image (top-left), captured image without micro mirrorcup (top-right), and captured image with micro mirrorcup (bottom). b–e) Reproduced with permission.[49] Copyright 2017, The Optical Society. f–h) Reproduced with permission.[33] Copyright 2019, National Academy of Sciences. i–k) Reproduced with permission.[34] Copyright 2018, The Optical Society. l–n) Reproduced with permission.[44] Copyright 2015, National Academy of Sciences.

high dynamic range (≈94.3 dB) imaging (Figure 5e, right) and also detect polarized light (Figure 5e, right).

Depth sensing is an important function in augmented and virtual reality applications. To obtain depth information with

**ADVANCED
SCIENCE NEWS**
www.advancedsciencenews.com

**ADVANCED
MATERIALS
TECHNOLOGIES**
www.advmattechnol.de

a conventional imaging system, additional information (i.e., perspective and motion) or additional optical components (i.e., structured light and stereo vision) are required.[116,117] Furthermore, optical defocusing that determines the depth has been demonstrated to reduce the amount of depth computation.[7,118] Similarly, the layered retina of a jumping spider proposes a novel depth perception method by capturing two different focused images with a single imaging device.[37] Considering the focusing mechanism of the human eye, it can detect an object only at one focused distance; however, the eye of a jumping spider can detect objects in different focal planes (Figure 5f). Hence, the jumping spider can obtain depth information with a single eye. Guo et al. developed a jumping-spider-eye-inspired metalens—a phase plate designed to focus light[33] (Figure 5g). The metalens is designed to incorporate the phase profiles of two off-axis lenses with different in-focus distances on a shared aperture. As a result, two differently defocused images can be captured simultaneously with a single shot (Figure 5h). The depth information can be extracted by computing the point spread function with two different focal plane images. The prototype of the depth sensor using a millimeter-scale metalens produces the depth value over a range of 10 cm with a single measurement.

In multispectral imaging, the images that are within certain wavelength ranges are captured. The wavelength can be separated by filters or by instruments that are sensitive to specific wavelengths (i.e., vis, IR, and UV). Garcia et al. developed a high-resolution multispectral imaging device using a photonic crystal structure that was inspired by the eye of a morph butterfly[34] (Figure 5i). The tapetal structure, which is comprised of alternating stacked layers of air and cytoplasm, functions as an interference filter. To mimic this tapetal structure, the thin films of SiO_2 and TiO_2 were alternatively deposited on a customized CMOS image sensor array, which generated photocurrent in the near-IR (NIR) and vis light regions (Figure 5j). The individual filters were optimized to accomplish 60% and 80% transmissions[34] of the vis and NIR lights, respectively. The image sensor was demonstrated by imaging a 4T1 breast cancer model under a surgical light illumination of 60 kLux and a laser light excitation power[34] of 5 mW cm$^{-1[2]}$ at a wavelength of 785 nm, which confirms its multispectral imaging capability (Figure 5k).

Most of the scotopic vision systems still adhere to the electronic amplifying method. However, the elephant nose fish adopts a different amplifying approach, a microoptical method to enhance its light detection performance. The retina of the elephant nose fish utilizes the microcups with reflecting photonic crystal sidewalls to collect and amplify the incident light (Figure 5l). Liu et al. demonstrated an optical strategy to improve the ability to collect light for imaging in low-intensity light[44] (Figure 5m). Each microcup is a glass microstructure with two opposite facets enclosed by four parabolic sidewalls that are coated with reflecting aluminum (Figure 5n). The incoming light from the large facet (input port) is concentrated on the small facet (output port) by a sidewall, thereby increasing the light intensity. A conventional image sensor with the bio-inspired nano-micro structure can detect additional light information. The novel bio-inspired artificial visions reviewed in this section have provided many new opportunities for the development of next-generation multifunctional imaging systems.

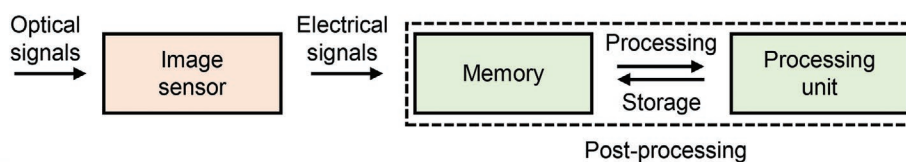## 3. Neuromorphic Image Processing Devices

The image data acquired by the image sensor array can be processed for the recognition of a specific object in the image. This back-end image processing technology has shown a rapid progress with the advent of novel applications of image sensors, including machine vision.[31] For example, the implementation of deep learning algorithms using an ANN has achieved significant success in terms of processing the unstructured image data.[28] However, the conventional von-Neumann architecture, in which the central data processing unit and memory unit are physically separated,[23,24] is not optimal for processing the massive image data that are acquired from an external image sensor[26] (**Figure 6**a). This has resulted in the development of a neuromorphic computing architecture based on synaptic devices that are inspired by human brain.[119] Such electronic synapses have an appropriate device structure for parallel processing of massive unstructured data (i.e., electrical signals) obtained from the image sensor[120] (Figure 6b). More recently, a novel concept of the neuromorphic device that integrates the synaptic and photodetecting functions in a single unit (a neuromorphic vision sensor) has been proposed[5,29–31] (Figure 6c). In this chapter, we review these neuromorphic image processing devices such as the electronic synapses and neuromorphic vision sensors. The important technological advances in the electronic synapses and neuromorphic vision sensors along with their detailed specifications such as device type, array size, and main features are summarized in **Table 1**.

3.1. Electronic Synapse

The memristor is a two-terminal device, and its resistance state depends on the history of current passed through the device.[11] The memristor can be applied to artificial intelligence (AI) in the form of in-memory computing for eliminating the von-Neumann bottleneck and to deep-learning accelerators for implementing vector-matrix multiplication.[119] When the memristor is fabricated into a crossbar array (i.e., electronic synapses), it can efficiently compute a large amount of vector-multiplication tasks using its programmable conductance. This resembles the working mechanism of the network of biological synapses in a human brain.[121] Such a memristor crossbar array has been a successful hardware implementation of the ANN and has shown unique advantages in the processing of the massive unstructured image data.[24] Furthermore, the electronic synapse has a simpler system configuration than the conventional processing system[122] (Figure 6b; i).
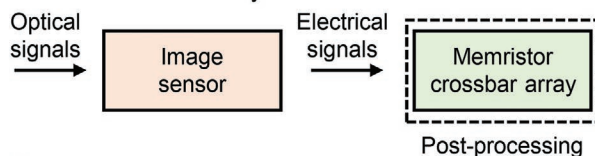
Despite recent advances in the memristor such as resistive random-access memory (RRAM), there are remaining technological challenges, such as poor CMOS compatibility,[123] crosstalk issue between memristors in the array,[124] and difficult bidirectional analog resistance modulation,[124] that have hindered the development of a large-area array of the memristor for the neuromorphic computing.[24,123,124] Recently, several researches to address these issues have been conducted and the corresponding studies have been reported.[24,123,124] For example, using a fully CMOS compatible fabrication process, conductive metal oxide with stable switching characteristics,

**ADVANCED
SCIENCE NEWS**

www.advancedsciencenews.com

**ADVANCED
MATERIALS
TECHNOLOGIES**

www.advmattechnol.de
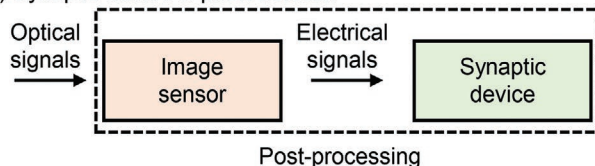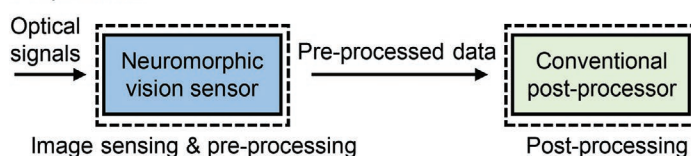
Figure 6. a) Block diagram of the image processing flow using the conventional image sensor and the conventional von-Neumann a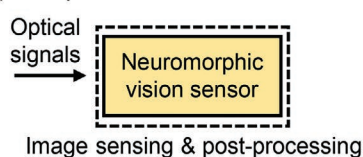rchitecture. b) Block diagram of the image processing flow using the electronic synapse based on the i) memristor crossbar array, or ii) the synaptic device and photodetector. c) Block diagram of the image processing flow using the neuromorphic vision sensor based on the i) pre-processor, or ii) the post-processor.

and integrating transistors, a high-density and large-scale RRAM array with an improved bidirectional analog switching capability can be developed.[124]

For example, Yao et al. developed a neuromorphic device with a structure of one transistor and one resistive memory[124] (i.e., 1T1R). Further, an array of 1024 cells with 128 rows and 8 columns was fabricated using this device structure (**Figure 7**a). The device exhibited symmetrical I–V curves (Figure 7b) and bidirectional conductance changes in response to the pulsed voltage inputs (i.e., set and reset operation) (Figure 7c), which is ideal for the efficient neuromorphic computing and pattern classification. Two operation schemes (i.e., with and without write-verify operation) were analyzed, exhibiting trade-offs in terms of converging speed, recognition accuracy, and energy consumption (Figure 7d). With the write-verify operation that can reduce the resistance variation between each cell, a system with a faster recognition speed, higher recognition accuracy, and lower energy consumption can be demonstrated. In

contrast, without the write-verify operation, although the recognition rate is slightly lower, the system operation could be simplified. In both the schemes, a remarkably lower energy consumption was achieved compared to a conventional system using the Intel Xeon Phi processor.

For the stable and uniform operation of the memristor crossbar arrays, individual switching element or external wiring are required; however, it can hinder the realization of high-density neuromorphic networks. In this context, a device-level improvement can be helpful for implementing high-density memristor crossbar arrays. Prezioso et al. reported a transistor-free memristor crossbar array[125] (12 × 12) (Figure 7e,f). The memristor consists of stacked oxide films (Al_2O_3/TiO_{2-x}) (Figure 7g inset) and shows non-linear I–V curves (Figure 7g). The device showed an on/off ratio of >10^4, high nonlinearity, a switching endurance of >5000 cycles, and an estimated memory retention of >10 years at room temperature. The memristor crossbar array, which is a high-density neural network

ADVANCED
SCIENCE NEWS
www.advancedsciencenews.com

ADVANCED
MATERIALS
TECHNOLOGIES
www.advmattechnol.de

Table 1. Specifications of various neuromorphic devices in terms of the device type, device configuration, array size, and their main features.

Device type	Device configuration	Array size	Main features	Ref.
Electronic synapse	TiN/TaO$_x$/HfAl$_y$O$_x$/TiN	128 × 8	Face classification	[124]
	Pt/Ti/TiO$_{2-x}$/Al$_2$O$_3$/Pt/Ta	12 × 12	Pattern classification	[125]
	W/WO$_x$/Au/Pd	32 × 32	Sparse coding	[25]
	Organic heterojunction photosensor + Ferroelectric dielectric/organic FET	5 × 6	Ultra-flexible, color-perception	[126]
	CdSe photosensor + a-IGZO TFT	3 × 3	Environment adaptation	[26]
	h-BN/WSe$_2$ +h-BN/WCL/WSe$_2$	Single pixel	Color mixed pattern recognition	[120]
Neuromorphic vision sensor	a-IGZO TFT	Single pixel	Major synaptic functions	[29]
	a-IGZO TFT	Single pixel	Pattern recognition	[131]
	Graphene-perovskite QD FET	Single pixel	Facial recognition	[132]
	Pd/MoO$_x$/ITO ORRAM	8 × 8	Pattern recognition	[30]
	MoS$_2$ phototransistor	31 pixels	Curved image sensor, pattern recognition	[28]
	MoS$_2$ phototransistor	32 × 32	Pattern recognition	[31]
	WSe$_2$ phototransistor	3 × 3	Classifier, autoencoder	[130]

(NN) capable of bidirectional conductance changes, can implement the single-layer perceptron. For example, the 3 × 3 black and white input patterns were classified into three letters ("z," "v," and "n") through analog vector-matrix multiplications. The output signals of the target letters were larger than those of the other letters (Figure 7h).

As another practical machine vision application, Sheridan et al. applied a WO$_x$-based memristor crossbar array (Figure 7i) to the implementation of the sparse coding for the efficient feature extraction in the object recognition process.[25] The desired conductance states can be programmed by redistributing ions in the WO$_x$ memristor (Figure 7j). Furthermore, the matrix operation of the 32 × 32 crossbar array can be achieved by the Kirchhoff's law (Figure 7k). Using the trained dictionary elements, the input greyscale image (Figure 7l) can be reconstructed with the reduced complexity (Figure 7m). In particular, a 4 × 4 patch that is a part of the original image can be clearly reconstructed with the increasing iteration number (Figure 7n). Moreover, the same procedure can be applied to other parts of the image for the complete reconstruction of the image. The successful hardware implementation of the sparse coding algorithm was confirmed.

When the synaptic devices are directly connected to the image sensors in one chip, the chip-to-chip communication can be replaced with the device-to-device communication.[120] Therefore, since the electrical signals from the photodetectors can be transported to the synaptic device by the intra-chip communication, the data communication speed can be significantly enhanced[120,126] (Figure 6b; ii). In addition, when the synaptic device is combined with the photodetector, diverse optical signals such as the incident light with various intensities or colors can be used as input parameters for the synaptic device.[26,120] The output electrical signals from the photodetectors can be used as the input signals for the synaptic devices.[126]

For example, Wang et al. realized such a device concept by integrating a ferroelectric synaptic device with a photodetecting element[126] (**Figure 8**a,b). The top-gated three-terminal synaptic device consists of P(VDF-TrFE)/P(VP-EDMAEMAES)

as a dielectric layer and P(IID-BT) as a channel material. The tow-terminal photodetecting device, connected in series with a phthalocyanine load resistor, consists of PTCDI-C8/VOPc as a photoabsorbing layer. The gate voltage of the synaptic device is regulated by the voltage divider circuit of the photodetecting device and the load resistor. Three kinds of synaptic plasticity, such as STP, LTP, and ferroelectric-LTP, were demonstrated. The gate voltage (V_g) was modulated according to the wavelength, intensity, and frequency of the incident light. The STP behavior is observed when V_g is lower than the coercive voltage (V_c). More frequent voltage pulses lead to more electrochemical doping, which corresponds to the electrochemical-LTP. When V_g exceeds V_c, the ferroelectric-LTP is achieved. The postsynaptic current of the ferroelectric-LTP lasts longer than that of the electrochemical-LTP. The ultra-flexibility of a light-triggered organic neuromorphic device (LOND) enables the device to conformally attach on a hemispherical surface (Figure 8c). In the case of green light spikes that trigger the ferroelectric characteristics, the LOND exhibits the LTP, in which 65% of the original input signal is maintained for 1800 s (Figure 8d).

A similar voltage dividing strategy but a different device structure made of different materials was reported by Kwon et al. They demonstrated the environment-adaptable visual perception using a synaptic device with a photodetector.[26] The device consists of an IGZO-based load transistor, a CdSe-based photosensor, and an IGZO-based ionotronic synaptic transistor (Figure 8e). The ionotronic synaptic transistor has a gate dielectric layer that consists of a sodium (Na)-incorporated aluminum oxide solid-state electrolyte. When the photodetector is irradiated with light, its channel resistance decreases by three orders of magnitude compared to the dark state, thereby resulting in increased bias spike (V_{spike}). The bias spike V_{spike} is calculated as $V_{spike} = V_{Drain} \cdot R_{load}/(R_{photosensor} + R_{load})$. If a small V_{spike} is applied to the synaptic device, mobile Na$^+$ ions move to the interface between the channel and the dielectric layer. As a result, electrons are induced in the channel, and an excitatory postsynaptic current (EPSC) is generated. However, the current disappears in 5 s due to rapid backward diffusion of the
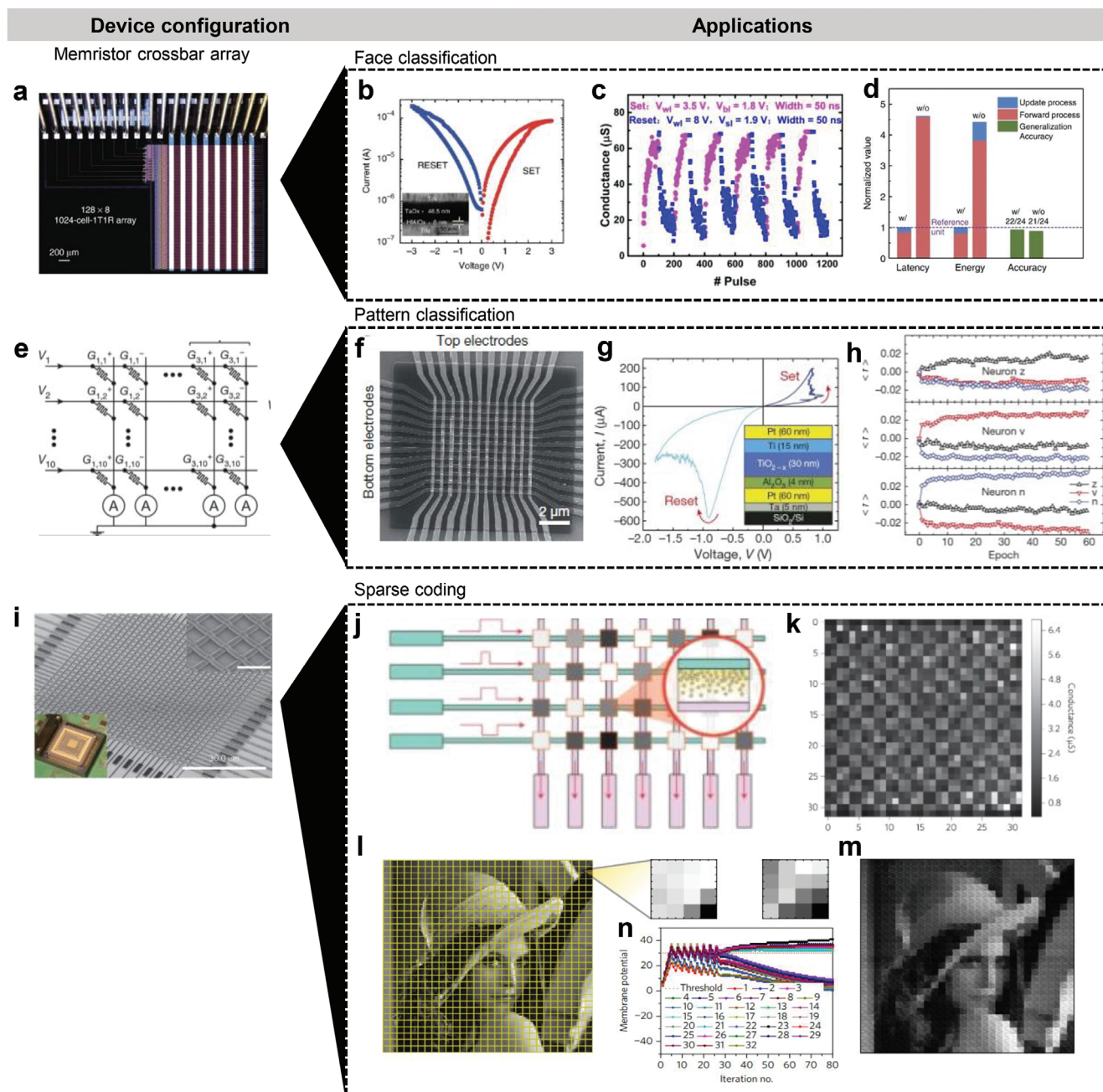
Figure 7. Electronic synapses based on the memristor crossbar array. a) The micrograph of the 1024-cell-1T1R array for face classification. b) *I–V* characteristic curve of a 1T1R device for the SET and RESET process. The inset shows a cross-sectional transmission electron microscope (TEM) image of the device. c) Conductance change behavior under a series of SET and RESET cycles. d) Comparison between with (w/) and without (w/o) the write-verify operation in terms of latency, energy consumption, and accuracy. e) Schematic circuit diagram of the memristor crossbar array for pattern classification. f) 12 × 12 memristor crossbar array based on Al_2O_3/TiO_{2-x} stacks. g) I–V characteristic curve of a memristor device for the SET and RESET process. The inset shows a cross-sectional view of the device. h) Experimental results of pattern classification tasks. i) Scanning electron microscope (SEM) image of the memristor crossbar array for sparse coding. j) Schematic illustration of the memristor crossbar array. k) 32 × 32 programmed chequerboard pattern with a patch size of 2 × 2. l) Original image for the image processing task using the memristor crossbar array. m) Reconstructed image. n) Graph that shows membrane potentials of the synaptic device as a function of the iteration number. a–d) Reproduced with permission.[124] Copyright 2017, Springer Nature. e–h) Reproduced with permission.[125] Copyright 2015, Springer Nature. i–n) Reproduced with permission.[25] Copyright 2017, Springer Nature.

Na^+ ions, which corresponds to the STP (Figure 8f). If V_{spike} is large, electrochemical doping occurs, generating a long-lasting current, which corresponds to the LTP (Figure 8g). A 3 × 3 array of the device was used to demonstrate the adaptation of the

human eye to strong and weak lights (i.e., photopic and scotopic adaptation) (Figure 8h).

In another example, a synaptic device with a photodetector (Figure 8i) was used in the pattern and color recognition
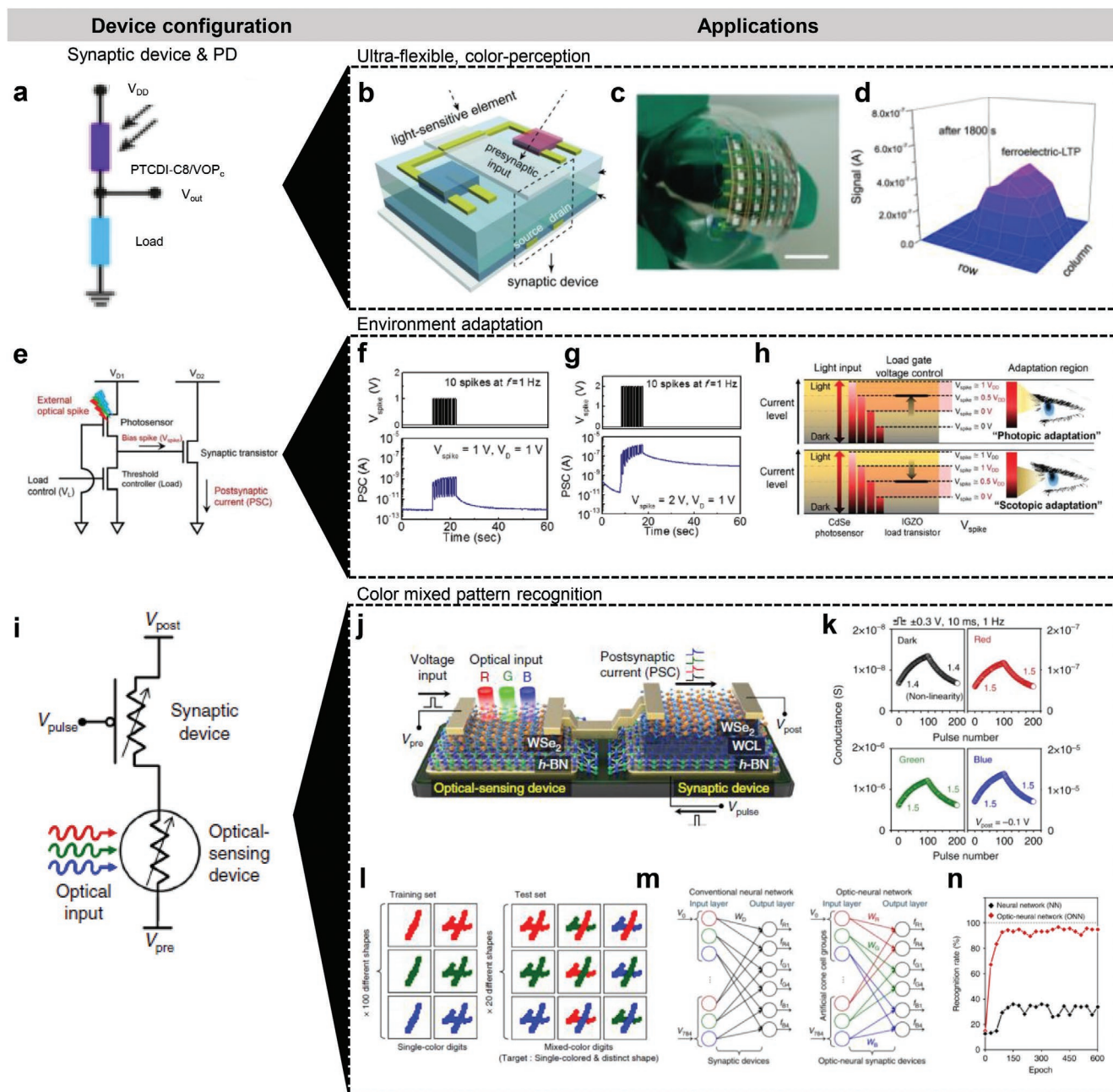
**ADVANCED
SCIENCE NEWS**

www.advancedsciencenews.com

**ADVANCED
MATERIALS
TECHNOLOGIES**

www.advmattechnol.de

Figure 8. Electronic synapse integrated with the photodetector. a) Schematic circuit diagram of an ultra-flexible light-triggered organic neuromorphic device (LOND) for color-perception. b) Schematic 3D illustration of LOND. c) Photograph of the LOND array transferred to a hemisphere. Scale bar, 7.5 mm. d) Current signal after 1800 s, showing the ferroelectric-LTP behavior of the LOND array triggered by a green-light. e) Schematic circuit diagram of a light-adjustable optoelectronic neuromorphic device array. f,g) EPSC dynamics of the synaptic transistor with f) $V_{spike} = 1$ V and g) $V_{spike} = 2$ V. h) The photopic adaptation (top) and scotopic adaptation (bottom) which emulate the human visual perception system. i) Schematic circuit diagram of an optic-neural synapse (ONS) for the recognition of color-mixed patterns. j) Schematic illustration of the optical-sensing device based on h-BN/WSe$_2$ and synaptic device based on h-BN/WCL/WSe$_2$. k) Conductance change behavior as a function of the pulse number under light of different colors. l) Numeric pattern images for the training and testing datasets consisting of single-color digits and mixed-color digits, respectively. m) Conventional neural network based on synaptic devices (left) and optic-neural network based on ONS devices (right). n) Recognition rate of neural network (NN) and optic-neural network (ONN) as a function of the number of training epochs. a–d) Reproduced with permission.[126] Copyright 2018, Wiley-VCH Verlag GmbH & Co. KGaA. e–h) Reproduced with permission.[26] Copyright 2019, Wiley-VCH Verlag GmbH & Co. KGaA. i–n) Reproduced with permission.[120] Copyright 2018, Springer Nature.

tasks.[120] The photodetecting device that consists of a heterostructure of h-BN and WSe$_2$ converts the optical signals (i.e., red ($\lambda = 655$ nm), green ($\lambda = 532$ nm), and blue ($\lambda = 405$ nm))

into the pre-synaptic electrical signals. Further, the pre-synaptic electrical signals control the postsynaptic current of the synaptic device (Figure 8j). The top surface of the h-BN layer

**ADVANCED
SCIENCE NEWS**
www.advancedsciencenews.com

**ADVANCED
MATERIALS
TECHNOLOGIES**
www.advmattechnol.de

is treated by O_2 plasma, which serves as a weight control layer (WCL). The applied voltage pulses result in electron trapping at the WCL-WSe$_2$ interface. Such trapping and de-trapping mechanisms enable the linear weight change, while maintaining the stable conductance state (Figure 8k). Using the device parameters extracted from the training (Figure 8l left), the color and pattern or the color-mixed pattern (Figure 8l, right) were successfully recognized. The performance, in terms of recognition accuracy, of the synaptic device with a photodetector (i.e., optical NN; ONN) was compared to that of a conventional NN (Figure 8m). With the same training epochs, the success rate of the ONN was higher than that of the NN (Figure 8n).

3.2. Neuromorphic Vision Sensor

Despite recent progresses in the neuromorphic devices, the electronic synapses still require additional image sensors to acquire raw image data and perform image-based processing tasks. This inevitably causes the system-level complexity and significant amount of data communication.[30] Further, processing raw image data requires a significant amount of computing, which consumes large amounts of energy and time.[28] Therefore, for fast processing and low power consumption, it is required to reduce the size of the raw image data.[127–129] Thus, the approach to integrate the photodetectors and neuromorphic devices as a single device has been proposed for high-efficiency and high-speed data processing.[28–31] Such an integration also helps in miniaturizing the size of the machine vision system. Such devices are called neuromorphic vision sensors (Figure 6c).

There are two types of neuromorphic vision sensors. One is the neuromorphic vision sensor that generates pre-processed electrical signals, which can be sent to the post-processing unit for image recognition[28,30] (Figure 6c; i). The pre-processed electrical signals require significantly less computation load in the post-processing unit than the unprocessed raw image data; hence, the entire processing efficiency, in terms of the computation load and processing time, can be increased.[28,30] The other is the neuromorphic vision sensor that performs the optical sensing and post-processing in one device[31,130] (Figure 6c; ii). In contrast to the neuromorphic vision sensor with only a pre-processor, a neuromorphic vision sensor equipped with post-processor can self-process the image recognition.[31,130] This can reduce the system-level complexity, minimize the amount of data communication, and eventually enhance the efficiency of the entire image recognition process.

As a sample device that could emulate the synaptic behaviors responsive to the optical input pulses, a photon-triggered neuromorphic device based on amorphous oxide semiconductors (AOSs) has been reported.[29] The AOS absorbs UV light, and the two-terminal device has a persistent photoconductivity under UV irradiation. The unique feature of this device is that the decay time of the photocurrent is long; hence, its photoconductivity can last over an extended period of time. Such a persistent photoconductivity is due to the excess carrier generation caused by the photo-induced ionized oxygen vacancies (i.e., VO$^+$ or VO^{2+}) (**Figure 9**a). Photon-triggered neuromorphic current responses (STP and LTP) can be obtained by controlling the photon energy and the frequency of the optical input pulses

(Figure 9b,c, respectively). Furthermore, the STDP was confirmed by two synaptic devices connected in series (Figure 9d). The connection strength between the adjacent devices increased with the decreasing time interval between the pre-synaptic and postsynaptic currents. The symmetrical shape of STDP characteristics was observed, which plays an important role in the learning and memorizing functions of the device.

In addition, analog synaptic potentiation and depression can be achieved by employing the combined stimulation of electrical voltage and optical pulses. Using the same AOS materials, but a different device structure, Duan et al. reported a three-terminal amorphous IGZO thin-film phototransistor[131] (Figure 9e). The device uses both the electrical voltage and optical pulses for the modulation of drain current. The current response was similar to the typical synaptic devices, which emulates the synaptic potentiation and depression as well as the major synaptic functions (i.e., STP and LTP) (Figure 9f). The optical pulse increases the current (i.e., EPSC), while the electrical pulse decreases the current (i.e., inhibitory postsynaptic current) (Figure 9g). A convolutional NN (CNN) was applied to the device for pattern recognition in the MNIST benchmark dataset. The recognition accuracy of the synaptic device reached 95.99%, which is comparable to that of the numerical simulation (i.e., 98.69%) (Figure 9h).

Instead of oxide thin films, Pradhan et al. developed a photosensitive neuromorphic transistor using organic-inorganic halide perovskite quantum dots (PQDs) and graphene[132] (Figure 9i). The structure of graphene-PQDs promotes efficient charge generation by PQDs and excellent charge transport by graphene, thereby resulting in high responsivity and detectivity of 1.4×10^8 AW^{-1} and 4.72×10^{15} Jones, respectively, at 430 nm.[132] The photon-triggered memory effect based on the number of input optical pulses was also characterized, and the synaptic current responses such as STP (Figure 9j) and LTP (Figure 9k) were observed. Long-term depression can be also generated by applying electrical pulses (Figure 9l). The neuromorphic phototransistor array can be applied in facial recognition (Figure 9m). The synaptic device generated the synaptic weight of each pixel in the form of a conductance state. When the summation of the postsynaptic currents exceeds the threshold, the output spike signal is generated. The synaptic weights are updated by the training and learning algorithms, and eventually, the features extracted from the original input images were obtained (Figure 9n).

Based on these photon-triggered synaptic characteristics, neuromorphic vision sensors that can perform both the imaging and pre-processing of the acquired image data were developed. For example, Zhou et al. developed a neuromorphic vision sensor based on the optoelectronic RRAM [30] (ORRAM). A simple two-terminal structure of Pd/MoO$_x$/ITO (**Figure 10**a) exhibited light-tunable non-volatile switching characteristics between the high-resistance state (HRS) and low-resistance state (LRS) (Figure 10b). When the MoO$_x$ thin film in the HRS is irradiated with UV light, protons (H$^+$) are generated by the reaction between the photogenerated holes and the water molecules in the MoO$_x$ thin film to form H$_y$MoO$_x$, which changes the resistance state of the device from the HRS to the LRS (Figure 10c, left). When an electrical field is applied to the device, the protons drift from the MoO$_x$ thin film to the Pd electrode, which returns the resistance state of the device to

**ADVANCED
SCIENCE NEWS**

www.advancedsciencenews.com

**ADVANCED
MATERIALS
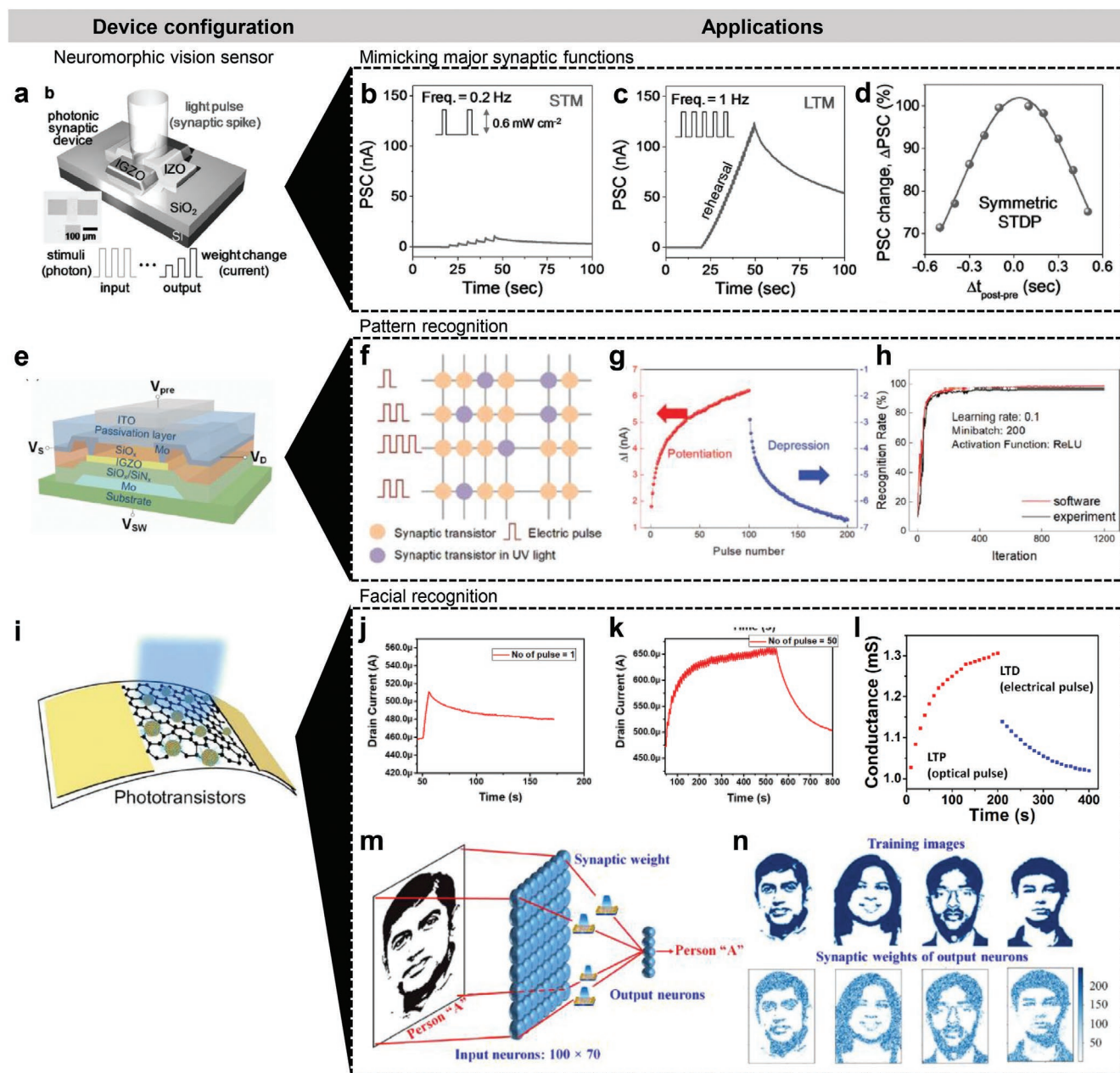TECHNOLOGIES**

www.advmattechnol.de

Figure 9. Neuromorphic vision sensor. a) Schematic illustration of the IGZO-based photonic neuromorphic device that can mimic major synaptic functions. Postsynaptic current behavior showing b) short-term memory and c) long-term memory. d) Postsynaptic current change between the presynaptic and postsynaptic devices as a function of the time interval, indicating symmetric spike-timing-dependent plasticity (STDP). e) Schematic illustration of the a-IGZO artificial synapse for pattern recognition. f) Schematic diagram of the synaptic transistor array of which the synaptic weights are modulated by the electrical pulses and UV light pulses. g) Analog synaptic behaviors of the device as a function of pulse number. h) Comparison of the recognition rate using software and that using the device for the MNIST benchmark task as a function of the iteration number. i) Schematic illustration of the phototransistor based on the G-PQD superstructure for facial recognition. Transient characteristic curve of the device showing j) short-term plasticity, and k) long-term plasticity, l) Conductance change of the device as a function of time. m) Schematic diagram of the neural network for face recognition. n) Training images (top) and corresponding synaptic weights of output artificial neurons (bottom). a–d) Reproduced with permission.[29] Copyright 2018, Wiley-VCH Verlag GmbH & Co. KGaA. e–h) Reproduced with permission.[131] Copyright 2019, Royal Society of Chemistry. i–n) Reproduced with permission.[132] Copyright 2020, American Association for the Advancement of Science.

the HRS from the LRS (Figure 10c, right). Using this mechanism, the original image could be pre-processed into an image with higher contrast and lesser noise (Figure 10d). The pre-processed image was sent to the post-processing unit. The image

recognition with ORRAM showed a higher accuracy than that without ORRAM (Figure 10e).

In another example, Choi et al. developed a curved neuromorphic image sensor array using a MoS$_2$-organic

**ADVANCED
SCIENCE NEWS**

www.advancedsciencenews.com

**ADVANCED
MATERIALS
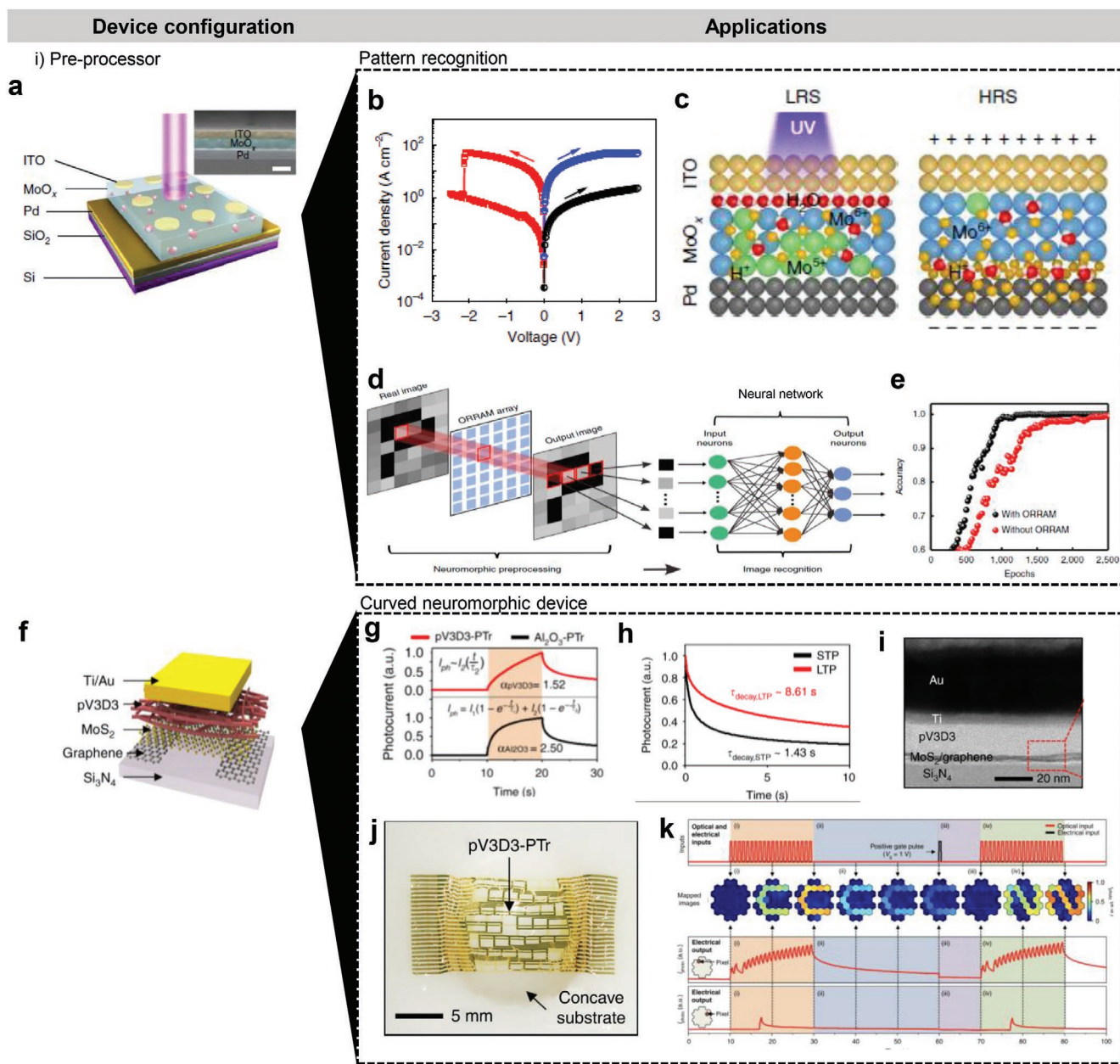TECHNOLOGIES**

www.advmattechnol.de

Figure 10. Neuromorphic vision sensors for pre-processing tasks. a) Schematic illustration of optoelectronic resistive random access memory (ORRAM) for pattern recognition. b) *I–V* characteristic curve of ORRAM for the SET and RESET process. The black and blue lines indicate the voltage sweeping behavior before and after the removal of UV illumination, respectively. The red line indicates the voltage sweeping behavior. c) Schematic illustration showing resistive switching mechanism of ORRAM. d) Schematic diagram showing overall image recognition process using ORRAM. e) The comparison of the recognition accuracy of system with ORRAM and without ORRAM as a function of epochs. f) Schematic illustration of the neuromorphic image sensor based on the MoS_2-organic heterostructure. g) Transient characteristic curve of pV3D3-PTr (red line) and Al_2O_3-PTr (black line). h) Photocurrent behaviors for short-term plasticity (black line) and long-term plasticity (red line). i) Cross-sectional TEM image of pV3D3-PTr. j) Photograph of the curved neuromorphic image sensor array (cNISA) transfer-printed onto the concave substrate. k) Demonstration of image pre-processing using cNISA. a–e) Reproduced with permission.[30] Copyright 2019, Springer Nature. f–k) Reproduced with permission.[28] Copyright 2020, Springer Nature.

heterostructure[28] (Figure 10f). The unique feature of this device is that its system design is inspired by a human eye with a single lens and a curved retina. In addition to the photon-induced neuromorphic function, the system complexity can be significantly decreased. The neuromorphic phototransistor exhibited the quasi-linear time-dependent

photocurrent generation and prolonged photocurrent decay (Figure 10g). The charge trapping at the interface between MoS_2 and poly(1,3,5-trimethyl-1,3,5-trivinyl cyclotrisiloxane) (pV3D3) resulted in the synaptic plasticity (i.e., STP and LTP) (Figure 10h). The ultrathin device with the thickness of ≈2 µm and intrinsically soft materials, such as graphene, MoS_2,

**ADVANCED
SCIENCE NEWS**

www.advancedsciencenews.com

**ADVANCED
MATERIALS
TECHNOLOGIES**

www.advmattechnol.de

and pV3D3 (Figure 10i), enabled the device mounted on the hemispherical surface (Figure 10j). Further, the neuromorphic image sensor array was integrated with a plano-convex lens, which can efficiently acquire an image and pre-process the acquired image data from extremely noisy optical inputs (Figure 10k). The afterimage (C-shaped image) can be erased by applying a positive gate pulse, and a new imaging and pre-processing step (N-shaped image) can be conducted.

Recently, neuromorphic vision sensors that can detect and post-process the input image data in a single device have been developed.[31] The phototransistor array based on 2D materials (i.e., MoS_2) can be applied to the post-processing and pre-processing tasks. Using large-area MoS_2 monolayer grown by metal-organic chemical vapor deposition, Jang et al. demonstrated a 32×32 MoS_2 phototransistor array, which is applicable to the machine vision (**Figure 11**a). Using the persistent
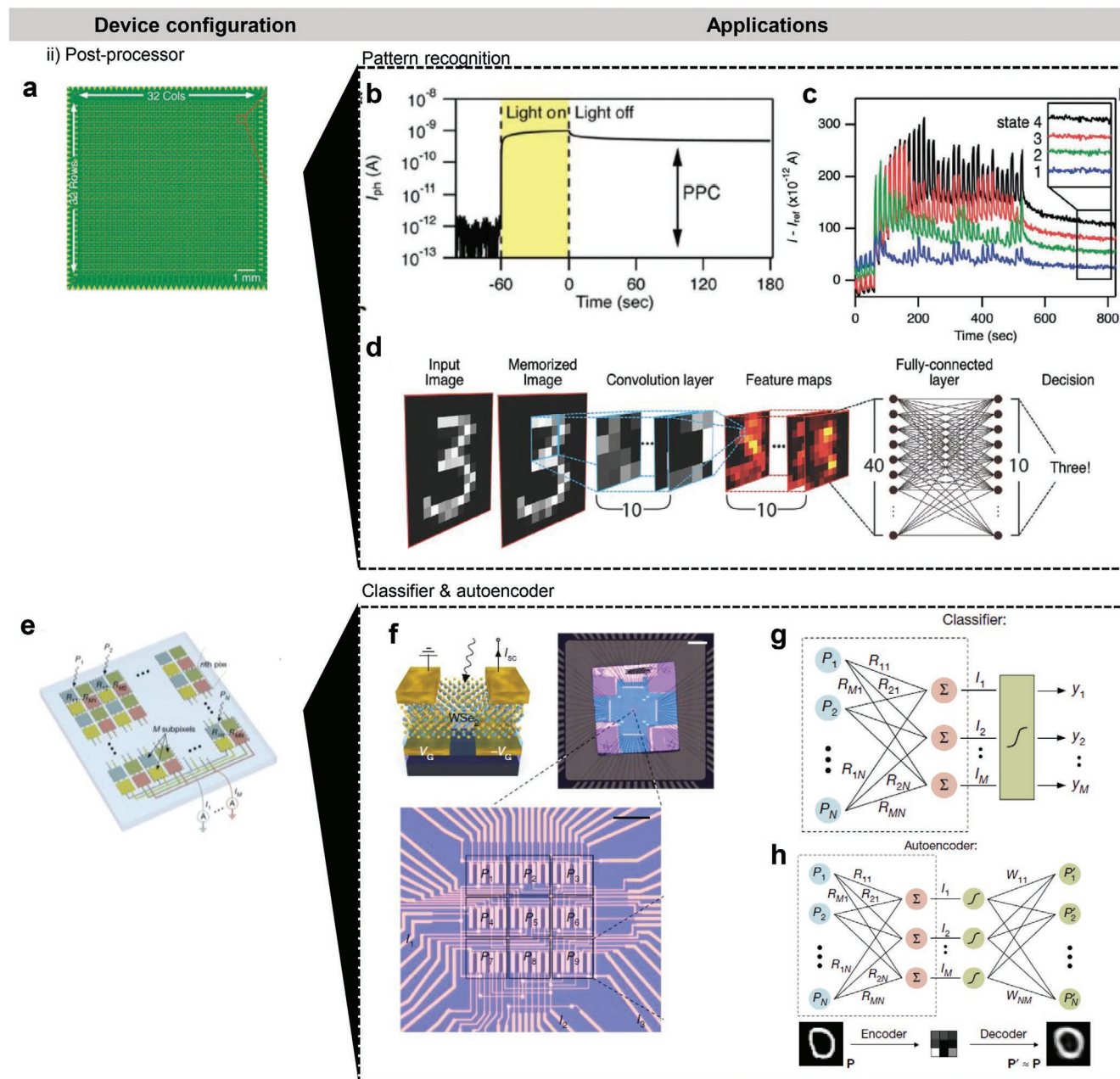

Figure 11. Neuromorphic vision sensors for post-processing tasks. a) Optical microscopy image of the 32×32 MoS_2 photo-FET crossbar array for pattern recognition. b) Transient characteristic curve of MoS_2 photo-FET. c) Transient characteristic curve showing the formation of optically programmed states after ≈40 iteration cycles. d) Schematic diagram showing the overall image recognition process using the MoS_2 photo-FET crossbar array. e) Schematic illustration of an image sensor array using the 2D material based neural network for applications as a classifier or an autoencoder. f) Schematic illustration (top left), macroscopic image (top right), and microscope image (bottom) of the WSe_2 photodiode. g,h) Diagrams showing operation schemes of the g) classifier and h) the autoencoder. a–d) Reproduced with permission.[31] Copyright 2020, Wiley-VCH Verlag GmbH & Co. KGaA. e–h) Reproduced with permission.[130] Copyright 2020, Springer Nature.

ADVANCED
SCIENCE NEWS
www.advancedsciencenews.com

ADVANCED
MATERIALS
TECHNOLOGIES
www.advmattechnol.de

photoconductivity effects of the MoS$_2$ transistor (Figure 11b), main functions of the human visual recognition system (i.e., optical sensing, memory, and recognition function) were emulated in this device. When the optical input is applied to the phototransistor array, the persistent photocurrent is generated, and the conductance of each pixel is determined by the light dosage (Figure 11c). Further, the vector-matrix multiplications are conducted using the stored conductance of each pixel for the image recognition process. For example, a 13 × 13 pixelated input image ("3") was first detected and memorized by the device. Using the stored conductance values, the device executed a series of the CNN algorithms and decision making through analog vector-multiplication (Figure 11d). The neuromorphic vision sensor could recognize 1000 MNIST images with 94% accuracy.

Using the photoresponsivity instead of the persistent photoconductivity of the 2D material, the post-processing of the image data for ultrafast machine vision applications could be achieved. Mennel et al. reported an ANN based on a photodiode array using a 2D material (WSe$_2$).[130] The device could both detect the input image and post-process the image data (Figure 11e). Similar to the electronic synapses that can perform the analog vector-multiplication using the applied voltage, conductance change, and electrical current, the p-n junction photodiode array performed the analog vector-multiplication using the light power, responsivity change, and photocurrent (Figure 11f). Two machine vision applications (i.e., classifier and autoencoder) were demonstrated using the device (Figure 11g,h, respectively). The supervised learning and unsupervised training algorithms were applied to perform the post-processing. Compared to the software-based image data processing, the neuromorphic vision sensor exhibited similar classifier performances in terms of accuracy and loss. Furthermore, the autoencoder could be demonstrated with the assistance of a decoder in external electronics. The original images were first encoded with the analog vision sensor, and then decoded into the reconstructed forms by the external electronics.

4. Conclusion and Future Prospects

Recent advances in the research and development of the image acquisition and processing devices were summarized in this review. Multifunctional image acquisition systems inspired by the geometrical features of natural eyes and novel computing architectures inspired by the NN in the human brain have been reviewed. The integration of both the front-end image acquisition and back-end image processing functions in a single device can significantly enhance the system-level efficiency of image recognition. Such novel approaches can be beneficial for the development of the advanced machine vision devices. These bio-inspired artificial imaging systems and neuromorphic image processing devices are a significant step toward the next-generation electronics. However, there are some remaining challenges for both the bio-inspired artificial vision and the neuromorphic processing devices that require further studies and researches.

First, the geometrical structures of biological eyes provided insights on the miniaturization of optical systems using the

GRIN lens, tunable iris, and curved image sensor array.[50–52,54] However, practical application of bio-inspired imaging systems is challenging since the trade-offs between the high resolution and high curvature of the image sensor array still exist. Therefore, to achieve a high-resolution image sensor array with a high curvature, new materials such as ultrathin and soft materials (e.g., MoS$_2$ and graphene) must be introduced.[40,80] New fabrication methods, such as 3D device processing techniques (e.g., device fabrication directly on a hemispherical platform), can also facilitate the implementation of the bio-inspired curved imaging system.[80] Although novel fabrication methods were developed, mimicking of natural eyes still has limitations due to initial phase of optimization. In 3D growth method, many potential pixels on curved platforms were implemented. However, there is an issue of addressing to carry the signal for imaging. To maximize geometrical advantage of the natural eye, not only the structural aspect in natural eye, but also a method to efficiently transmit signals should be studied. Meanwhile, the photonic crystals and microstructures in a natural eye can provide useful guidelines for designing unique optical components (e.g., layered retina, orthogonal microvilli, and tapetum lucidum), which allow multifunctional imaging such as depth detection, polarization, and invisible lights (i.e., UV and IR lights) in addition to the conventional high-resolution imaging.[33,34,37,44] In order to bring functional benefits in nature eye, not only photonic structure, but also geometric structures must be studied simultaneously to make full use of optical properties in natural eye (i.e., microcup structure with photonic crystal). These bio-inspired components can find novel applications such as in unconventional surgical tools and military devices.

In the neuromorphic image processing, the electronic synapses based on the memristor crossbar array have resolved the issue of energy inefficiency, which occurs in the massive parallel data processing (e.g., vector multiplications) using the conventional von-Neumann architecture. However, the memristor crossbar array has limitations such as the sneak-path issue during its array operation.[123] Suppressing the sneak-path current would significantly reduce the crosstalk and allow the development of a high-density array. In addition, despite the advent of the neuromorphic vision sensor that integrates the sensing and processing capabilities, most of the devices still need additional electrical modulations for learning and training.[28] Furthermore, the applications of the neuromorphic vision sensors are still limited to specific areas, in contrast to the software-based neuromorphic computations.[133,134] Also, the large-scale integration of the neuromorphic computing architecture is still challenging due to the high cost, reliability, noise, and accuracy issues.[134] Therefore, further research is essential to completely utilize the advantages of the optically-driven neuromorphic computing platforms.

[1] H. Deng, X. Gao, M. Ma, Y. Li, H. Li, J. Zhang, X. Zhong, *Opt. Express* **2018**, *26*, 12455.

[2] S. B. Powell, R. Garnett, J. Marshall, C. Rizk, V. Gruev, *Sci. Adv.* **2018**, *4*, eaao6841.

[3] D. S. Jeong, C. S. Hwang, *Adv. Mater.* **2018**, *30*, 1704729.

[4] T. Ohno, T. Hasegawa, T. Tsuruoka, K. Terabe, J. K. Gimzewski, M. Aono, *Nat. Mater.* **2011**, *10*, 591.

[5] F. Zhou, J. Chen, X. Tao, X. Wang, Y. Chai, *Research* **2019**, *2019*, 9490413.

[6] G. J. Lee, C. Choi, D. Kim, Y. M. Song, *Adv. Funct. Mater.* **2018**, *28*, 1705202.

[7] Q. Guo, E. Alexander, T. Zickler, in *Proc. IEEE Int. Conf. Computer Vision*, IEEE, Piscataway, NJ **2017**, pp. 966–974.

[8] A. Brueckner, J. Duparré, R. Leitel, P. Dannberg, A. Bräuer, A. Tünnermann, *Opt. Express* **2010**, *18*, 24379.

[9] M. S. Kim, G. J. Lee, H. M. Kim, Y. M. Song, *Sensors* **2017**, *17*, 1774.

[10] G. J. Lee, W. Il Nam, Y. M. Song, *Opt. Laser Technol.* **2017**, *96*, 50.

[11] Q. F. Xia, J. J. Yang, *Nat. Mater.* **2019**, *18*, 518.

[12] Y. van de Burgt, A. Melianas, S. T. Keene, G. Malliaras, A. Salleo, *Nat. Electron.* **2018**, *1*, 386.

[13] Z.-D. Luo, X. Xia, M.-M. Yang, N. R. Wilson, A. Gruverman, M. Alexe, *ACS Nano* **2020**, *14*, 746.

[14] M. J. Cox, *Ophthalmic Physiol. Opt.* **2001**, *21*, 426.

[15] C. Posch, T. Serrano-Gotarredona, B. Linares-Barranco, T. Delbruck, *Proc. IEEE* **2014**, *102*, 1470.

[16] M. F. Land, *Contemp. Phys.* **1988**, *29*, 435.

[17] V. Lakshminarayanan, M. K. Parthasarathy, *J. Mod. Opt.* **2016**, *0340*, 1.

[18] A. Bruckner, J. Duparre, P. Dannberg, A. Brauer, A. Tunnermann, *Opt. Express* **2007**, *15*, 11922.

[19] J. Duparré, P. Dannberg, P. Schreiber, A. Bräuer, A. Tünnermann, *Appl. Opt.* **2005**, *44*, 2949.

[20] P. Lin, C. Li, Z. R. Wang, Y. N. Li, H. Jiang, W. H. Song, M. Y. Rao, Y. Zhuo, N. K. Upadhyay, M. Barnell, Q. Wu, J. J. Yang, Q. F. Xia, *Nat. Electron.* **2020**, *3*, 225.

[21] P. Gkoupidenis, D. A. Koutsouras, G. G. Malliaras, *Nat. Commun.* **2017**, *8*, 15448.

[22] S. Seo, J.-J. Lee, H.-J. Lee, H. W. Lee, S. Oh, J. J. Lee, K. Heo, J.-H. Park, *ACS Appl. Electron. Mater.* **2020**, *2*, 371.

[23] Y.-N. Zhong, T. Wang, X. Gao, J.-L. Xu, S.-D. Wang, *Adv. Funct. Mater.* **2018**, *28*, 1800854.

[24] M. A. Zidan, J. P. Strachan, W. D. Lu, *Nat. Electron.* **2018**, *1*, 22.

[25] P. M. Sheridan, F. X. Cai, C. Du, W. Ma, Z. Y. Zhang, W. D. Lu, *Nat. Nanotechnol.* **2017**, *12*, 784.

[26] S. M. Kwon, S. W. Cho, M. Kim, J. S. Heo, Y. Kim, S. K. Park, *Adv. Mater.* **2019**, *31*, 1906433.

[27] S. H. Jo, T. Chang, I. Ebong, B. B. Bhadviya, P. Mazumder, W. Lu, *Nano Lett.* **2010**, *10*, 1297.

[28] C. Choi, J. Leem, M. S. Kim, A. Taqieddin, C. Cho, K. W. Cho, G. J. Lee, H. Seung, H. J. Bae, Y. M. Song, T. Hyeon, N. R. Aluru, S. Nam, D.-H. Kim, *Nat. Commun.* **2020**, *11*, 5934.

[29] M. Lee, W. Lee, S. Choi, J.-W. Jo, J. Kim, S. K. Park, Y.-H. Kim, *Adv. Mater.* **2017**, *29*, 1700951.

[30] F. C. Zhou, Z. Zhou, J. W. Chen, T. H. Choy, J. L. Wang, N. Zhang, Z. Y. Lin, S. M. Yu, J. F. Kang, H. S. P. Wong, Y. Chai, *Nat. Nanotechnol.* **2019**, *14*, 776.

[31] H. Jang, C. Liu, H. Hinton, M. Lee, H. Kim, M. Seol, H. Shin, S. Park, D. Ham, *Adv. Mater.* **2020**, *32*, 2002431.

[32] Y. Deng, H. Duan, *IEEE Trans. Aerosp. Electron. Syst.* **2018**, *54*, 3125.

[33] Q. Guo, Z. J. Shi, Y. W. Huang, E. Alexander, C. W. Qiu, F. Capasso, T. Zickler, *Proc. Natl. Acad. Sci. U. S. A.* **2019**, *116*, 22959.

[34] M. Garcia, C. Edmiston, T. York, R. Marinov, S. Mondal, N. Zhu, G. P. Sudlow, W. J. Akers, J. Margenthaler, S. Achilefu, R. G. Liang, M. A. Zayed, M. Y. Pepino, V. Gruev, *Optica* **2018**, *5*, 413.

[35] X. Lin, J. Wu, G. Zheng, Q. Dai, *Biomed. Opt. Express* **2015**, *6*, 3179.

[36] T. Martinez, D. Wick, S. Restaino, *Opt. Express* **2001**, *8*, 555.

[37] T. Nagata, M. Koyanagi, H. Tsukamoto, S. Saeki, K. Isono, Y. Shichida, F. Tokunaga, M. Kinoshita, K. Arikawa, A. Terakita, *Science* **2012**, *335*, 469.

[38] S. B. Rim, P. B. Catrysse, R. Dinyari, K. Huang, P. Peumans, *Opt. Express* **2008**, *16*, 4965.

[39] H. C. Ko, M. P. Stoykovich, J. Z. Song, V. Malyarchuk, W. M. Choi, C. J. Yu, J. B. Geddes, J. L. Xiao, S. D. Wang, Y. G. Huang, J. A. Rogers, *Nature* **2008**, *454*, 748.

[40] C. Choi, M. K. Choi, S. Liu, M. S. Kim, O. K. Park, C. Im, J. Kim, X. Qin, G. J. Lee, K. W. Cho, M. Kim, E. Joh, J. Lee, D. Son, S.-H. Kwon, N. L. Jeon, Y. M. Song, N. Lu, D.-H. Kim, *Nat. Commun.* **2017**, *8*, 1664.

[41] Y. M. Song, Y. Xie, V. Malyarchuk, J. Xiao, I. Jung, K.-J. Choi, Z. Liu, H. Park, C. Lu, R.-H. Kim, R. Li, K. B. Crozier, Y. Huang, J. A. Rogers, *Nature* **2013**, *497*, 95.

[42] D. Floreano, R. Pericet-Camara, S. Viollet, F. Ruffier, A. Bruckner, R. Leitel, W. Buss, M. Menouni, F. Expert, R. Juston, M. K. Dobrzynski, G. L'Eplattenier, F. Recktenwald, H. A. Mallot, N. Franceschini, *Proc. Natl. Acad. Sci. U. S. A.* **2013**, *110*, 9267.

[43] L. C. Kogos, Y. Li, J. Liu, Y. Li, L. Tian, R. Paiella, *Nat. Commun.* **2020**, *11*, 1637.

[44] H. W. Liu, Y. G. Huang, H. Jiang, *Proc. Natl. Acad. Sci. U. S. A.* **2016**, *113*, 3982.

[45] M. S. Kim, G. J. Lee, C. Choi, M. S. Kim, M. Lee, S. Y. Liu, K. W. Cho, H. M. Kim, H. Cho, M. K. Choi, N. S. Lu, Y. M. Song, D. H. Kim, *Nat. Electron.* **2020**, *3*, 546.

[46] S. Thiele, K. Arzenbacher, T. Gissibl, H. Giessen, A. M. Herkommer, *Sci. Adv.* **2017**, *3*, e1602655.

[47] S. Potier, M. Mitkus, T. J. Lisney, P.-F. Isard, T. Dulaurent, M. Mentek, R. Cornette, D. Schikorski, A. Kelber, *Sci. Rep.* **2020**, *10*, 6133.

[48] D. Keum, K.-W. Jang, D. S. Jeon, C. S. H. Hwang, E. K. Buschbeck, M. H. Kim, K.-H. Jeong, *Light: Sci. Appl.* **2018**, *7*, 80.

[49] M. Garcia, T. Davis, S. Blair, N. Cui, V. Gruev, *Optica* **2018**, *5*, 1240.

[50] G. Zuccarello, D. Scribner, R. Sands, L. J. Buckley, *Adv. Mater.* **2002**, *14*, 1261.

[51] H. Zeng, O. M. Wani, P. Wasylczyk, R. Kaczmarek, A. Priimagi, *Adv. Mater.* **2017**, *29*, 1701814.

[52] L. Dong, A. K. Agarwal, D. J. Beebe, H. R. Jiang, *Nature* **2006**, *442*, 551.

[53] S. Z. Ji, M. Ponting, R. S. Lepkowicz, A. Rosenberg, R. Flynn, G. Beadie, E. Baer, *Opt. Express* **2012**, *20*, 26746.

**ADVANCED
SCIENCE NEWS**

www.advancedsciencenews.com

**ADVANCED
MATERIALS
TECHNOLOGIES**

www.advmattechnol.de

[54] G. Beadie, J. S. Shirk, A. Rosenberg, P. A. Lane, E. Fleet, A. R. Kamdar, Y. Jin, M. Ponting, T. Kazmierczak, Y. Yang, A. Hiltner, E. Baer, *Opt. Express* **2008**, *16*, 11540.

[55] S. Ji, K. Yin, M. Mackey, A. Brister, M. Ponting, E. Baer, *Opt. Eng.* **2013**, *52*, 112105.

[56] H. M. Kim, G. J. Lee, M. S. Kim, Y. M. Song, *J. Visualized Exp.* **2018**, *136*, e57502.

[57] E. K. Lee, R. K. Baruah, J. W. Leem, W. Park, B. H. Kim, A. Urbas, Z. Ku, Y. L. Kim, M. A. Alam, C. H. Lee, *Adv. Mater.* **2020**, *32*, 2004456.

[58] I. W. Jung, J. L. Xiao, V. Malyarchuk, C. F. Lu, M. Li, Z. J. Liu, J. Yoon, Y. G. Huang, J. A. Rogers, *Proc. Natl. Acad. Sci. U. S. A.* **2011**, *108*, 1788.

[59] B. Guenter, N. Joshi, R. Stoakley, A. Keefe, K. Geary, R. Freeman, J. Hundley, P. Patterson, D. Hammon, G. Herrera, E. Sherman, A. Nowak, R. Schubert, P. Brewer, L. Yang, R. Mott, G. McKnight, *Opt. Express* **2017**, *25*, 13010.

[60] O. Iwert, D. Ouellette, M. Lesser, B. Delabre, in *High Energy, Optical, and Infrared Detectors for Astronomy V* (Eds: A. D. Holland, J. W. Beletic), SPIE, Bellingham, WA **2012**, p. 84531W.

[61] K. Zhang, Y. H. Jung, S. Mikael, J.-H. Seo, M. Kim, H. Mi, H. Zhou, Z. Xia, W. Zhou, S. Gong, Z. Ma, *Nat. Commun.* **2017**, *8*, 1782.

[62] T. Wu, S. S. Hamann, A. C. Ceballos, C.-E. Chang, O. Solgaard, R. T. Howe, *Microsyst. Nanoeng.* **2016**, *2*, 16019.

[63] C.-H. Lin, D.-S. Tsai, T.-C. Wei, D.-H. Lien, J.-J. Ke, C.-H. Su, J.-Y. Sun, Y.-C. Liao, J.-H. He, *ACS Nano* **2017**, *11*, 10230.

[64] W. Lee, Y. Liu, Y. Lee, B. K. Sharma, S. M. Shinde, S. D. Kim, K. Nan, Z. Yan, M. Han, Y. Huang, Y. Zhang, J.-H. Ahn, J. A. Rogers, *Nat. Commun.* **2018**, *9*, 1417.

[65] G. Shin, I. Jung, V. Malyarchuk, J. Song, S. Wang, H. C. Ko, Y. Huang, J. S. Ha, J. A. Rogers, *Small* **2010**, *6*, 851.

[66] K. Sim, S. Chen, Z. W. Li, Z. Y. Rao, J. S. Liu, Y. T. Lu, S. Jang, F. Ershad, J. Chen, J. L. Xiao, C. J. Yu, *Nat. Electron.* **2019**, *2*, 471.

[67] K. Sim, Y. Li, J. Song, C. Yu, *Adv. Mater. Technol.* **2019**, *4*, 1800489.

[68] D. Son, J. Lee, S. Qiao, R. Ghaffari, J. Kim, J. E. Lee, C. Song, S. J. Kim, D. J. Lee, S. W. Jun, S. Yang, M. Park, J. Shin, K. Do, M. Lee, K. Kang, C. S. Hwang, N. S. Lu, T. Hyeon, D. H. Kim, *Nat. Nanotechnol.* **2014**, *9*, 397.

[69] J.-K. Song, D. Son, J. Kim, Y. J. Yoo, G. J. Lee, L. Wang, M. K. Choi, J. Yang, M. Lee, K. Do, J. H. Koo, N. Lu, J. H. Kim, T. Hyeon, Y. M. Song, D.-H. Kim, *Adv. Funct. Mater.* **2017**, *27*, 1605286.

[70] S. Choi, S. I. Han, D. Jung, H. J. Hwang, C. Lim, S. Bae, O. K. Park, C. M. Tschabrunn, M. Lee, S. Y. Bae, J. W. Yu, J. H. Ryu, S. W. Lee, K. Park, P. M. Kang, W. B. Lee, R. Nezafat, T. Hyeon, D. H. Kim, *Nat. Nanotechnol.* **2018**, *13*, 1048.

[71] S. Sunwoo, S. I. Han, H. Kang, Y. S. Cho, D. Jung, C. Lim, C. Lim, M. Cha, S. Lee, T. Hyeon, D. Kim, *Adv. Mater. Technol.* **2020**, *5*, 1900768.

[72] J. Lee, H. R. Cho, G. D. Cha, H. Seo, S. Lee, C.-K. Park, J. W. Kim, S. Qiao, L. Wang, D. Kang, T. Kang, T. Ichikawa, J. Kim, H. Lee, W. Lee, S. Kim, S.-T. Lee, N. Lu, T. Hyeon, S. H. Choi, D.-H. Kim, *Nat. Commun.* **2019**, *10*, 5205.

[73] K. W. Cho, S. J. Kim, J. Kim, S. Y. Song, W. H. Lee, L. Wang, M. Soh, N. Lu, T. Hyeon, B.-S. Kim, D.-H. Kim, *Nat. Commun.* **2019**, *10*, 4824.

[74] J. Kim, M. Lee, H. J. Shim, R. Ghaffari, H. R. Cho, D. Son, Y. H. Jung, M. Soh, C. Choi, S. Jung, K. Chu, D. Jeon, S.-T. Lee, J. H. Kim, S. H. Choi, T. Hyeon, D.-H. Kim, *Nat. Commun.* **2014**, *5*, 5747.

[75] S. Choi, H. Lee, R. Ghaffari, T. Hyeon, D. H. Kim, *Adv. Mater.* **2016**, *28*, 4203.

[76] J. Park, S. Choi, A. H. Janardhan, S.-Y. Lee, S. Raut, J. Soares, K. Shin, S. Yang, C. Lee, K.-W. Kang, H. R. Cho, S. J. Kim, P. Seo, W. Hyun, S. Jung, H.-J. Lee, N. Lee, S. H. Choi, M. Sacks, N. Lu, M. E. Josephson, T. Hyeon, D.-H. Kim, H. J. Hwang, *Sci. Transl. Med.* **2016**, *8*, 344ra86.

[77] H. Lee, T. K. Choi, Y. B. Lee, H. R. Cho, R. Ghaffari, L. Wang, H. J. Choi, T. D. Chung, N. S. Lu, T. Hyeon, S. H. Choi, D. H. Kim, *Nat. Nanotechnol.* **2016**, *11*, 566.

[78] J. Kim, D. Son, M. Lee, C. Song, J.-K. Song, J. H. Koo, D. J. Lee, H. J. Shim, J. H. Kim, M. Lee, T. Hyeon, D.-H. Kim, *Sci. Adv.* **2016**, *2*, e1501101.

[79] S. J. Kim, K. W. Cho, H. R. Cho, L. Wang, S. Y. Park, S. E. Lee, T. Hyeon, N. Lu, S. H. Choi, D. H. Kim, *Adv. Funct. Mater.* **2016**, *26*, 3207.

[80] L. L. Gu, S. Poddar, Y. J. Lin, Z. H. Long, D. Q. Zhang, Q. P. Zhang, L. Shu, X. Qiu, M. Kam, A. Javey, Z. Y. Fan, *Nature* **2020**, *581*, 278.

[81] C. Choi, Y. Lee, K. W. Cho, J. H. Koo, D.-H. Kim, *Acc. Chem. Res.* **2019**, *52*, 73.

[82] D. C. Kim, H. J. Shim, W. Lee, J. H. Koo, D. Kim, *Adv. Mater.* **2020**, *32*, 1902743.

[83] H. Joo, D. Jung, S. Sunwoo, J. H. Koo, D. Kim, *Small* **2020**, *16*, 1906270.

[84] C. Lim, Y. Shin, S. Hong, S. Lee, D. Kim, *Adv. Mater. Interfaces* **2020**, *7*, 1902170.

[85] G. D. Cha, W. H. Lee, C. Lim, M. K. Choi, D.-H. Kim, *Nanoscale* **2020**, *12*, 10456.

[86] J. G. Kim, N. Takama, B. J. Kim, H. Fujita, *J. Micromech. Microeng.* **2009**, *19*, 055017.

[87] H. Bian, Y. Wei, Q. Yang, F. Chen, F. Zhang, G. Du, J. Yong, X. Hou, *Appl. Phys. Lett.* **2016**, *109*, 221109.

[88] S. H. Park, R. Su, J. Jeong, S.-Z. Guo, K. Qiu, D. Joung, F. Meng, M. C. McAlpine, *Adv. Mater.* **2018**, *30*, 1803980.

[89] K. W. Cho, W. H. Lee, B.-S. Kim, D.-H. Kim, *Talanta* **2020**, *219*, 121269.

[90] J. H. Koo, J. Song, S. Yoo, S. Sunwoo, D. Son, D. Kim, *Adv. Mater. Technol.* **2020**, *5*, 2000407.

[91] G. D. Cha, T. Kang, S. Baik, D. Kim, S. H. Choi, T. Hyeon, D.-H. Kim, *J. Controlled Release* **2020**, *328*, 350.

[92] S. H. Sunwoo, S. I. Han, H. Joo, G. D. Cha, D. Kim, S. H. Choi, T. Hyeon, D. H. Kim, *Matter* **2020**, *3*, 1923.

[93] H. Joo, Y. Lee, J. Kim, J.-S. Yoo, S. Yoo, S. Kim, A. K. Arya, S. Kim, S. H. Choi, N. Lu, H. S. Lee, S. Kim, S.-T. Lee, D.-H. Kim, *Sci. Adv.* **2021**, *7*, eabd4639.

[94] C. Choi, M. K. Choi, T. Hyeon, D.-H. Kim, *ChemNanoMat* **2016**, *2*, 1006.

[95] D. Son, S. I. Chae, M. Kim, M. K. Choi, J. Yang, K. Park, V. S. Kale, J. H. Koo, C. Choi, M. Lee, J. H. Kim, T. Hyeon, D. H. Kim, *Adv. Mater.* **2016**, *28*, 9326.

[96] M. Kaltenbrunner, T. Sekitani, J. Reeder, T. Yokota, K. Kuribara, T. Tokuhara, M. Drack, R. Schwodiauer, I. Graz, S. Bauer-Gogonea, S. Bauer, T. Someya, *Nature* **2013**, *499*, 458.

[97] D. Akinwande, N. Petrone, J. Hone, *Nat. Commun.* **2014**, *5*, 5678.

[98] M. K. Choi, J. Yang, K. Kang, D. C. Kim, C. Choi, C. Park, S. J. Kim, S. I. Chae, T.-H. Kim, J. H. Kim, T. Hyeon, D.-H. Kim, *Nat. Commun.* **2015**, *6*, 7149.

[99] M. K. Choi, I. Park, D. C. Kim, E. Joh, O. K. Park, J. Kim, M. Kim, C. Choi, J. Yang, K. W. Cho, J. H. Hwang, J. M. Nam, T. Hyeon, J. H. Kim, D. H. Kim, *Adv. Funct. Mater.* **2015**, *25*, 7109.

[100] S. Lim, D. Son, J. Kim, Y. B. Lee, J. K. Song, S. Choi, D. J. Lee, J. H. Kim, M. Lee, T. Hyeon, D. H. Kim, *Adv. Funct. Mater.* **2015**, *25*, 375.

[101] M. K. Choi, O. K. Park, C. Choi, S. T. Qiao, R. Ghaffari, J. Kim, D. J. Lee, M. Kim, W. Hyun, S. J. Kim, H. J. Hwang, S. H. Kwon, T. Hyeon, N. S. Lu, D. H. Kim, *Adv. Healthcare Mater.* **2016**, *5*, 80.

[102] M. K. Choi, J. Yang, D. C. Kim, Z. Dai, J. Kim, H. Seung, V. S. Kale, S. J. Sung, C. R. Park, N. Lu, T. Hyeon, D.-H. Kim, *Adv. Mater.* **2018**, *30*, 1703279.

[103] M. F. Land, D. Nilsson, *Animal Eyes*, Oxford University Press, Oxford **2012**.

[104] Y. M. Song, H. G. Park, G. J. Lee, J. S. Park, in *Smart Sensors and Systems Innovation for Medical, Environmental, and IoT Applications*

**ADVANCED
SCIENCE NEWS**

www.advancedsciencenews.com

**ADVANCED
MATERIALS
TECHNOLOGIES**

www.advmattechnol.de

(Eds: C.-M. Kyung, H. Yasuura, Y. Liu, Y.-L. Lin), Springer, Cham **2017**, p. 157.

[105] K. Kim, K.-W. Jang, J.-K. Ryu, K.-H. Jeong, *Light: Sci. Appl.* **2020**, *9*, 28.

[106] J. Tanida, T. Kumagai, K. Yamada, S. Miyatake, K. Ishida, T. Morimoto, N. Kondou, D. Miyazaki, Y. Ichioka, *Appl. Opt.* **2001**, *40*, 1806.

[107] R. Horisaki, Y. Nakao, T. Toyoda, K. Kagawa, Y. Masaki, J. Tanida, *Opt. Rev.* **2009**, *16*, 241.

[108] M. K. Dobrzynski, R. Pericet-Camara, D. Floreano, *IEEE Sens. J.* **2012**, *12*, 1131.

[109] M. F. Land, *J. Opt. A: Pure Appl. Opt.* **2000**, *2*, R44.

[110] K. Bitsakos, C. Fermüller, *Biol. Cybern.* **2006**, *95*, 487.

[111] R. J. Lin, V.-C. Su, S. Wang, M. K. Chen, T. L. Chung, Y. H. Chen, H. Y. Kuo, J.-W. Chen, J. Chen, Y.-T. Huang, J.-H. Wang, C. H. Chu, P. C. Wu, T. Li, Z. Wang, S. Zhu, D. P. Tsai, *Nat. Nanotechnol.* **2019**, *14*, 227.

[112] R. Völkel, M. Eisner, K. J. Weible, *Microelectron. Eng.* **2003**, *67*, 461.

[113] M. Kreysing, R. Pusch, D. Haverkate, M. Landsberger, J. Engelmann, J. Ruiter, C. Mora-Ferrer, E. Ulbricht, J. Grosche, K. Franze, S. Streif, S. Schumacher, F. Makarov, J. Kacza, J. Guck, H. Wolburg, J. K. Bowmaker, G. von der Emde, S. Schuster, H.-J. Wagner, A. Reichenbach, M. Francke, *Science* **2012**, *336*, 1700.

[114] I. M. Daly, M. J. How, J. C. Partridge, S. E. Temple, N. J. Marshall, T. W. Cronin, N. W. Roberts, *Nat. Commun.* **2016**, *7*, 12140.

[115] M. Garcia, C. Edmiston, R. Marinov, A. Vail, V. Gruev, *Optica* **2017**, *4*, 1263.

[116] M. Z. Brown, D. Burschka, G. D. Hager, *IEEE Trans. Pattern Anal. Mach. Intell.* **2003**, *25*, 993.

[117] S. T. Barnard, M. A. Fischler, *ACM Comput. Surv.* **1982**, *14*, 553.

[118] E. Alexander, Q. Guo, S. Koppal, S. J. Gortler, T. Zickler, *Int. J. Comput. Vis.* **2018**, *126*, 1062.

[119] A. Mehonic, A. Sebastian, B. Rajendran, O. Simeone, E. Vasilaki, A. J. Kenyon, *Adv. Intell. Syst.* **2020**, *2*, 2000085.

[120] S. Seo, S.-H. Jo, S. Kim, J. Shim, S. Oh, J.-H. Kim, K. Heo, J.-W. Choi, C. Choi, S. Oh, D. Kuzum, H.-S. P. Wong, J.-H. Park, *Nat. Commun.* **2018**, *9*, 5106.

[121] M. Kumar, D. Ban, S. M. Kim, J. Kim, C. Wong, *Adv. Electron. Mater.* **2019**, *5*, 1900467.

[122] B. C. Jang, S. Kim, S. Y. Yang, J. Park, J.-H. Cha, J. Oh, J. Choi, S. G. Im, V. P. Dravid, S.-Y. Choi, *Nano Lett.* **2019**, *19*, 839.

[123] L. Shi, G. Zheng, B. Tian, B. Dkhil, C. Duan, *Nanoscale Adv.* **2020**, *2*, 1811.

[124] P. Yao, H. Wu, B. Gao, S. B. Eryilmaz, X. Huang, W. Zhang, Q. Zhang, N. Deng, L. Shi, H.-S. P. Wong, H. Qian, *Nat. Commun.* **2017**, *8*, 15199.

[125] M. Prezioso, F. Merrikh-Bayat, B. D. Hoskins, G. C. Adam, K. K. Likharev, D. B. Strukov, *Nature* **2015**, *521*, 61.

[126] H. Wang, Q. Zhao, Z. Ni, Q. Li, H. Liu, Y. Yang, L. Wang, Y. Ran, Y. Guo, W. Hu, Y. Liu, *Adv. Mater.* **2018**, *30*, 1803961.

[127] Y. Wang, Z. Lv, J. Chen, Z. Wang, Y. Zhou, L. Zhou, X. Chen, S.-T. Han, *Adv. Mater.* **2018**, *30*, 1802883.

[128] Z. Lv, M. Chen, F. Qian, V. A. L. Roy, W. Ye, D. She, Y. Wang, Z. Xu, Y. Zhou, S. Han, *Adv. Funct. Mater.* **2019**, *29*, 1902374.

[129] S. Ham, S. Choi, H. Cho, S.-I. Na, G. Wang, *Adv. Funct. Mater.* **2019**, *29*, 1806646.

[130] L. Mennel, J. Symonowicz, S. Wachter, D. K. Polyushkin, A. J. Molina-Mendoza, T. Mueller, *Nature* **2020**, *579*, 62.

[131] N. Duan, Y. Li, H. C. Chiang, J. Chen, W. Q. Pan, Y. X. Zhou, Y. C. Chien, Y. H. He, K. H. Xue, G. Liu, T. C. Chang, X. S. Miao, *Nanoscale* **2019**, *11*, 17590.

[132] B. Pradhan, S. Das, J. Li, F. Chowdhury, J. Cherusseri, D. Pandey, D. Dev, A. Krishnaprasad, E. Barrios, A. Towers, A. Gesquiere, L. Tetard, T. Roy, J. Thomas, *Sci. Adv.* **2020**, *6*, eaay5225.

[133] A. Lugnan, A. Katumba, F. Laporte, M. Freiberger, S. Sackesyn, C. Ma, E. Gooskens, J. Dambre, P. Bienstman, *APL Photonics* **2020**, *5*, 020901.

[134] F. Zhou, Y. Chai, *Nat. Electron.* **2020**, *3*, 664.

Min Sung Kim received his B.S. in 2016 from the School of Chemical and Biological Engineering at Seoul National University, and he is now pursuing his Ph.D. in the School of Chemical and Biological Engineering at Seoul National University under the supervision of Prof. Dae-Hyeong Kim. His current research involves the fabrication of flexible optoelectronic devices for bio-inspired imaging systems and neuromorphic vision sensors.

Min Seok Kim received an M.S. in Electrical Engineering and Computer Science from Gwangju Institute of Science and Technology (GIST) in 2019 after a B.S. degree in Electronic Engineering from Pusan National University in 2017. He is currently a Ph.D. candidate in the School of Electrical Engineering and Computer Science at the GIST. His research includes multifunctional imaging system, advanced optoelectronic device.

Young Min Song received an M.S. and a Ph.D. in Information and Communications from the Gwangju Institute of Science and Technology (GIST) in 2006 and 2011, respectively, after a B.S. degree in Biomedical Engineering from Yonsei University in 2004. From 2011 to 2013, he was a postdoctoral research associate in the Department of Materials Science and Engineering at the University of Illinois at Urbana–Champaign. He is currently a professor in the School of Electrical Engineering and Computer Science at the GIST. His research includes multifunctional nanophotonics, advanced optoelectronic devices/systems, and bioinspired imaging applications.

Dae-Hyeong Kim received his B.S. in 2000 and his M.S. in 2002 from the School of Chemical Engineering at Seoul National University. He obtained his Ph.D. in 2009 from the Department of Materials Science and Engineering at the University of Illinois at Urbana–Champaign. Since he joined the faculty of the School of Chemical and Biological Engineering at Seoul National University in 2011, he has focused on stretchable electronics for bio-medical applications and optoelectronic devices.